REY A. OZIN

ier: Amsterdam,

2.

New York, 1977.
York, 1980, pp.

d.; International

am, 1981.
obs, P. A.; Van

ntertext Books:

05. Leschewski,

ng. 1970, *40*, 17.
and Molecular

322–328.
ichester, 1984.

tal Instrumental

M.; Pines, A. *J.*

; N. V.; Ovsian-

mission of the

CONTROLLING SOLID STATE REACTIONS VIA RATIONAL DESIGN OF SUPERLATTICE REACTANTS

Loreli Fister, Thomas Novet,
Christopher A. Grant, and David C. Johnson

Advances in the Synthesis and Reactivity of Solids
Volume 2, pages 155–234

ISBN: 1-55938-330-5

1. INTRODUCTION

1.1 The Importance of Solid State Synthesis

The synthesis of new materials has traditionally been a necessary precursor to the discovery of new chemical and physical phenomena. The discovery of large coercive-force magnets based upon iron–rare-earth–boron alloys [1,2] and high-temperature superconductivity in copper oxide materials [3] both illustrate this point—new compounds are the key to dramatic breakthroughs in materials properties. The recognition of this fact has led to a close coupling between the synthesis of a new compound and the investigation of its properties. Thirty years ago, new materials were often prepared simply for the sake of making new materials, and the investigation of a new compound's chemical and physical properties commonly lagged behind its structural determination by ten years or more [4]. Today, there is greater impetus to correlate physical properties with structure and composition. Increasingly, the preparation of new materials is driven by the desire to make compounds which have particular properties, and this in turn has led to increased interactions between synthesis and measurement groups.

The obvious challenge to the solid state chemist is the synthesis of new materials with desired or novel structures and physical properties. The increased interaction among theory, measurement, and synthesis has resulted in specific goals or targets for the synthetic community. The ability to design a set of compounds with a desired three-dimensional architecture to probe a particular phenomenon exists; unfortunately, the ability to prepare those desired new compounds upon demand does not.

Traditional solid state synthetic techniques produce thermodynamic reaction products. The two key synthetic steps in the formation of a compound with an extended structure from traditional high-temperature solid state reactions are interdiffusion of the reagents and nucleation of the extended structure. The high activation energies required for solid state diffusion cause mixing of the reactants to be the rate-limiting step in the reaction process. High reaction temperatures are typically used to overcome slow solid state diffusion while obtaining reasonable reaction rates. Elevated reaction temperatures permit any and all crystalline com-

pounds to nucleate and grow during the interdiffusion process. There is no control of the reaction intermediates. There is also no detailed understanding of interdiffusion or nucleation in "real" synthetic systems. Consequently, solid state chemists have had to settle for finding a set of experimental conditions under which the desired product is thermodynamically stable [5].

The traditional solid state synthetic approach differs substantially from that used by synthetic molecular chemists, who focus on kinetic approaches to desired products. Significantly, the details of the reaction mechanism are considered as important as the product itself. The reaction mechanism provides an important conceptual framework for the synthetic chemist, promoting an understanding of cause-and-effect relationships between changes in synthetic parameters and product distributions. This kinetic approach to synthesis has led to the great richness of small-molecule chemistry, highlighted by the isolation of structural and geometric isomers for materials with the same composition.

A similar, kinetic-based approach to the synthesis of extended solids permitting the preparation of metastable compounds is needed. The elucidation and use of a reaction mechanism for this kinetic approach would provide a systematic framework for solid state synthetic efforts. A kinetic approach would also permit the preparation of a host of new compounds which are currently impossible to prepare due to their thermodynamic instability with respect to other possible compounds. Synthetic targets made feasible by a kinetic approach include new compounds which are isostructural to known compounds having unusual physical properties, compounds which are stable only at low temperatures, and amorphous alloys. The preparation of "nano-engineered" materials, consisting of a composite of compounds of differing composition or structure interleaved on a tens of Ångstrom length scale is another, yet more challenging synthetic goal. The capability of preparing new compounds with desired structures on demand would greatly enhance interactions among synthesis, measurement, and theory.

Superlattices as reactants offer the potential to control the reaction pathway by engineering the structure of the initial superlattice. The diffraction patterns resulting from the regular repeat of electron density within the superlattice offer the possibility of exploring the initial stages of a solid state reaction before the formation of a crystalline compound at the reacting interfaces. The information obtained concerning the development of interfacial structure is of vital importance to develop a mechanism for solid state reactions which can be used to guide synthetic efforts. This chapter describes the progress we have made to date in these areas.

1.2. Overview

This chapter is organized into ten sections. Section 1 contains a brief introduction and this overview. Section 2 consists of a short review of the available literature on the mechanism of a solid state reaction. The accepted picture of solid state reactions in both the bulk state and in thin films is discussed, followed by the special

case of solid state amorphization reactions. We summarize this background section by proposing a simple model for the progression of a solid state reaction.

Section 3 of this chapter summarizes our synthetic strategy. We suggest that the key to obtaining kinetic control of a solid state reaction is to separate the reaction steps of diffusion and nucleation, accessing an amorphous reaction intermediate as a bulk material. Various routes to amorphous intermediates are then discussed in terms of their synthetic utility.

The remainder of the chapter is devoted to our synthetic approach, the use of ultrathin superlattices to derive a more general synthetic route to amorphous intermediates. Section 4 summarizes the important experimental variables which can be used to control the reactions of the initial superlattices. The techniques used to both prepare and characterize the superlattices made in our laboratory are discussed.

Section 5 discusses the analytical approaches used to characterize the initial superlattice reactants. The interpretation of superlattice diffraction patterns is discussed in detail, and the structural information obtained is contrasted with that obtained via other experimental techniques.

Section 6 summarizes the experimental approaches used to follow the solid state reactions occurring in the superlattices on annealing. The use of differential scanning calorimetry (DSC) and low-angle X-ray diffraction to follow the sequence of reaction events is discussed. Background pertaining to the interpretation of changes in the low-angle diffraction patterns with interdiffusion is presented. Several examples of interfacial reactions are given which provide support for the solid state reaction mechanism presented in Section 2.4. This section concludes with a summary of the inherent advantages of superlattices for the elucidation of solid state reaction mechanisms.

Section 7 presents examples of how the rational design of superlattice reactants permits the pathway of solid-state reactions to be controlled. The general utility of this synthetic route to prepare binary and ternary compounds directly via amorphous intermediates is demonstrated with specific examples.

The final sections of this chapter detail future directions and synthetic goals made possible by the development of this synthetic approach (Section 8), summarize the problems to date (Section 9), and acknowledge the support which made this research possible (last section).

2. BACKGROUND

2.1. Bulk Reactions

The simplest form of a bulk reaction involves mixing stoichiometric amounts of the desired elements, heating this mixture at high temperatures (1000°C) for many hours or days to overcome slow solid state diffusion, and then determining the product distribution via powder X-ray diffraction. This procedure is illustrated in

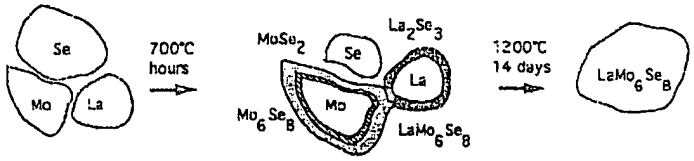

Figure 1. Schematic of the reaction of molybdenum, selenium, and lanthanum to form the ternary compound $LaMo_6Se_8$.

Figure 1 for the preparation of a ternary molybdenum selenide [6]. Such a reacting system is very complex, due to the existence of multiple crystalline compounds, a distribution of particle sizes and reacting grain boundaries, and the influence of defects upon diffusion rates. Interdiffusion of the elements and nucleation of products occur simultaneously. As a consequence of this complexity and the high reaction temperatures used, there is no control of the reaction pathway or of reaction intermediates [7].

The lack of control of a reaction pathway is a tremendous liability when attempting to prepare ternary and other higher-order compounds, as the desired ternary product must be thermodynamically more stable than any other compound at the reaction conditions. The rate of conversion of the crystalline binary intermediates to the desired ternary product can also inhibit the ability to prepare a pure compound. A further liability is the inability to follow the steps in the reaction with experimental probes. All the action in solid state reactions takes place at interfaces, and the small ratio of interfacial to bulk volume limits the applicability of most experimental techniques. The lack of a suitable probe of interfacial reactions combined with the inability to control the reactions make most solid state synthetic efforts an empirical procedure.

The complexity of typical reacting mixtures has thwarted efforts to determine reaction mechanisms *in situ*. One method of simplifying the above reaction is to restrict the interfacial region to a known location and geometry by creating a diffusion couple. A diffusion couple is made by placing two blocks of dissimilar materials in intimate contact with each other, resulting in a well-defined and planar interface. This geometry allows the study of the interdiffusion reaction as well as phase formation as a function of temperature and time. A schematic of an iron–silicon bulk diffusion couple both before and after prolonged heating is illustrated in Figure 2 [8].

The length scale of the product layers usually investigated via bulk diffusion couples is on the order of microns. As in traditional solid state preparative reactions, the interfacial reaction is diffusion limited. High reaction temperatures and long reaction times [8] are usually necessary as a result of the large activation energies for solid state diffusion. An undesirable consequence of these reaction conditions is that every thermodynamically stable binary compound in the phase diagram will nucleate and grow. The relative amounts of the various compounds will be

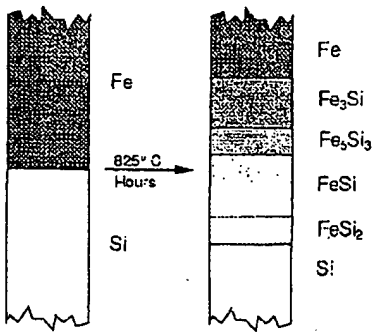

Figure 2. Schematic of a bulk iron–silicon diffusion couple after annealing for several hours at 825°C.

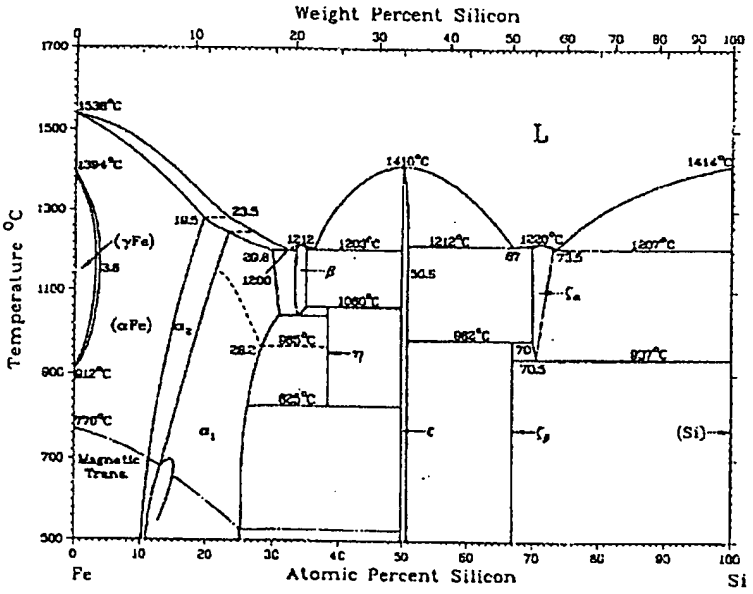

Figure 3. Binary phase diagram for iron and silicon.

determined by the diffusion rates of the elements through each of the compounds formed. Consequently, bulk diffusion couples have long been used to probe phase diagrams and to determine the existence of stable binary phases. A comparison of the above iron–silicon diffusion couple with the equilibrium phase diagram [9] in Figure 3 illustrates the utility of this technique for exploring equilibrium phase diagrams.

For bulk high-temperature reactions of elements, the heats of formation and the distribution of the thermodynamic products can usually be estimated from tabulated thermochemical data [10]. Rates of conversion of reactants to products could, in principle, be calculated from known diffusion coefficients and the reacting temperature. Little information is available, however, concerning the initial formation of products from reactants. Indirect evidence for the importance of this key synthetic step, the initial formation of product, has been obtained via studies of thin-film reactions.

c after

2.2. Thin-Film Reactions

In the 1970s and early 1980s several research groups began to explore the reaction of "thin-film" diffusion couples. This research was at first motivated by the economic importance of thin-film reactions in the semiconductor industry and subsequently driven by the observation that the products formed by heating thin films of transition metals deposited upon silicon substrates could be different than predicted from bulk reacting systems. These initial efforts focused on the reaction of metal–silicon and metal–metal systems.

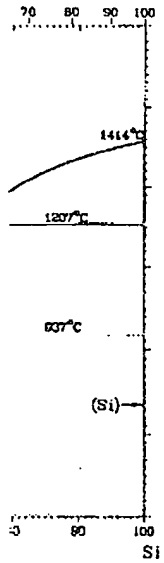

In a typical investigation, crystalline films of approximately 500 Å of each element were deposited to produce a diffusion couple [11–16]. This diffusion couple was subsequently annealed at temperatures of several hundred degrees Celsius to interdiffuse the elements. When the thickness of the individual layers was less than some critical distance, a compound was observed to nucleate at the interface and grow until it exhausted one of the reactants. Only then was another crystalline phase observed to nucleate at the compound/remaining element interface. This second compound grew until it exhausted the supply of compound or element. In this type of a reaction sequence, not all the compounds in the phase diagram were necessarily formed [17,18].

In a regime limited by length scale, diffusion and nucleation rates were found to alternately determine the progress of the reaction. The rate of growth of a particular phase, and hence the time scale of the reaction, was governed by diffusion rates. However, at these length scales, nucleation of a new phase did not occur until one of the reacting layers was consumed. Figure 4 illustrates the behavior observed in a prototypical thin-film diffusion couple, iron–silicon, as a function of temperature and time.

The sequential phase formation observed in these systems aroused considerable interest. Empirical rules were developed predicting the first compound formed at a reacting interface as well as the order of subsequent compound formation within

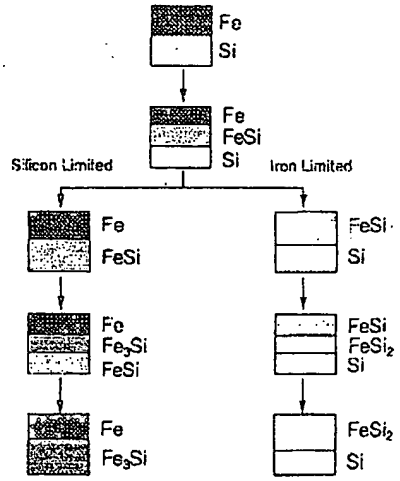

Figure 4. Schematic of the evolution of a thin-film iron–silicon diffusion couple as a function of temperature and time.

the developing diffusion couple. Walser and Bené compiled available data on binary silicides and empirically correlated the first phase formed in a thin-film diffusion couple with information obtained from bulk equilibrium phase diagrams. Their "first phase rule" states:

> The first compound nucleated in planar binary reaction couples is the most stable congruently melting compound adjacent to the lowest temperature eutectic on the bulk equilibrium phase diagram. [18]

The iron–silicon phase diagram shown in Figure 3 can be used to demonstrate this rule. The lowest melting eutectic in the phase diagram is at 34 at. % silicon. The congruent phase with the highest melting point adjacent to this eutectic is FeSi. FeSi has been experimentally determined to be the first phase which forms in a thin-film diffusion couple as shown schematically in Figure 4 [19].

Walser and Bené speculated that the physical basis for their rule was related to the composition of an amorphous region which they suggested might develop at the interface between two solid reactants. They reasoned that the composition of this amorphous intermediate would be close to that of the deepest eutectic, the most stable liquid in the phase diagram. From the amorphous alloy, the most likely phase to nucleate would be the one nearest in composition and local bonding to that of the amorphous intermediate. They also recognized that the energy change between the amorphous and crystalline states would be an important component of the

nucleation kinetics. They suggested that to zero order this energy change could be approximated by considering the melting point of the compounds close in composition to the proposed amorphous intermediate [17]. They empirically found that the congruently melting compound with the highest melting point closest in composition to the eutectic was formed in metal–silicon systems.

A similar rule predicting the second phase which nucleates has also been proposed [20]. It too is based on information found in bulk phase diagrams and states:

> The second phase formed is the compound with the smallest temperature difference between the liquidus curve and the peritectic (if the compound melts congruently, then this temperature difference is zero) that exists in the phase diagram between the composition of the first phase and the unreacted element.

This rule is also based on the assumption that an amorphous interfacial region develops, this time between the remaining element and the first phase formed. The authors speculate that a small difference in composition between the peritectic and the liquidus phase at the peritectic temperature yields a low-energy barrier for nucleation because only small compositional fluctuations are required for nucleation. More simply stated, the most likely phase to nucleate will be the one with the composition closest to that of the interfacial amorphous alloy.

The work on thin-film diffusion couples defined several important stages in the development of a bulk diffusion couple and identified important experimental parameters which affect the evolution of reacting solids. The key points are:

- the progression of a solid state reaction is affected by diffusion lengths;
- an amorphous interfacial alloy is a key reaction intermediate;
- composition of the amorphous alloy controls the crystalline product formed; and
- nucleation of this intermediate is the rate-limiting factor determining the sequence of products formed.

The next section discusses a special case of thin-film reactions, known as solid state amorphization reactions, where a bulk amorphous alloy is isolated as a reaction intermediate.

2.3. Solid State Amorphization Reactions

In 1983, Schwartz and Johnson observed that Au–La multilayer composites with crystalline elemental layers 300 Å thick interdiffused at low temperatures to form a homogeneous, amorphous alloy [21]. In a later publication, calorimetry and diffraction data were presented clearly demonstrating the formation of an amorphous intermediate from the interdiffusion reaction of crystalline nickel and crystalline zirconium layers [22]. The initial explanation of this reaction focused

on the anomalously large diffusion rate of nickel into zirconium, suggesting that crystallization was prevented by the lack of mobility of the zirconium atoms. Subsequent research has found that several metal–metal, metal–silicon, and metal–carbon systems also react at low temperatures via a solid state amorphization reaction in which anomalous diffusion is not a common feature [23]. Although various models have been proposed for predicting the occurrence of solid state amorphization reactions based upon thermodynamic and atomic size criteria [24–27], there is still considerable debate as to the underlying mechanism of these reactions.

Two surprising aspects of solid state amorphization reactions are the stability of the amorphous alloy with respect to the unreacted crystalline, elemental components and the inability of the system to nucleate a crystalline compound from the amorphous intermediate. The stability of the amorphous alloy with respect to the unreacted elements has been attributed to the large negative heat of mixing of the elements. In many of the solid state amorphization reactions investigated, the formation of the amorphous alloy produces a majority of the heat of formation of the final crystalline compound. The most studied solid state amorphization reaction, that of nickel and zirconium, illustrates this point well. Over 90% of the heat of formation of the final crystalline alloy is produced during the amorphization reaction. The remaining heat of formation is given off when the amorphous alloy crystallizes [22].

The distribution of the heat of formation of the compound between the mixing of the elements to form the amorphous alloy and the crystallization of the alloy supports Walser and Bené's suggestion that an amorphous alloy forms at the reacting interface as a precursor to the formation of a crystalline product. This reflects the importance of local geometry in the crystal structure of the final product. In the commonly studied intermetallic or metal–metalloid systems, the structure of the crystalline compound has both elements in high coordination states. The local structure in the crystalline solid is similar in coordination number to that proposed for liquid metals and results in the small observed heats of crystallization. In systems with a more anisotropic structure, a larger proportion of the heat evolved might be expected in the crystallization step, reflecting the larger change in structure from the amorphous alloy to the crystalline solid.

Although the crystalline product is more stable than the amorphous alloy, it is thought not to form due to kinetic limitations resulting from the existence of a nucleation barrier. A familiar analog is the behavior of a supersaturated solution which crystallizes rapidly upon the addition of a seed crystal. The amorphous solid formed at the interface between reacting solids can be thought of as a supersaturated "solution." The nucleation step involves the assemblage of the proper kinds of atoms via diffusion, structural rearrangement into intermediates, and the formation of stable nuclei upon which crystals can grow [28]. The transformation of the metastable, amorphous intermediate into a thermodynamically more stable crystalline product initially begins on a very small scale due to entropy considerations.

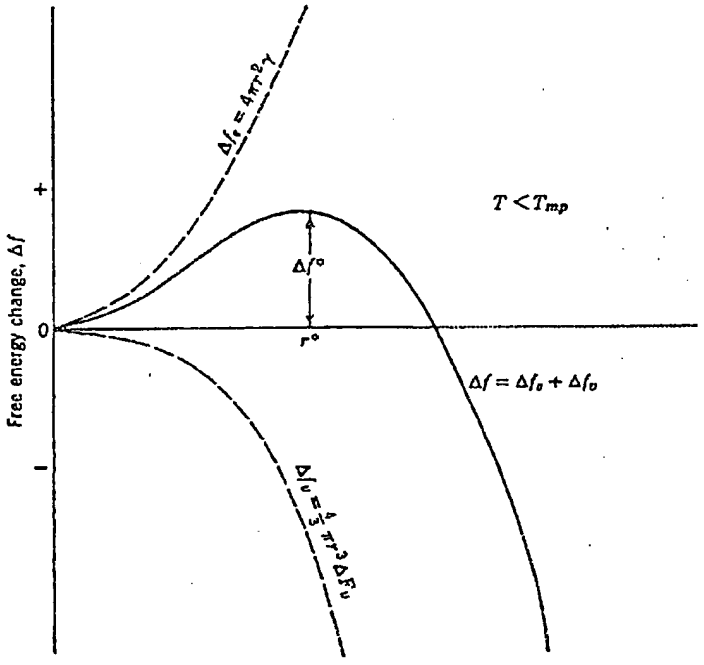

Figure 5. Radial dependence of the free energy for homogeneous nucleation of spherical nuclei from a homogeneous fluid.

Nucleation from a homogeneous fluid system provides a simple model for understanding factors which will affect nucleation within a solid matrix. Suppose a small region of a stable crystalline compound, referred to as an embryo, appears in the middle of a melt with stoichiometry identical to that of the crystalline compound. A free energy decrease, Δf_v per unit volume, would be expected as a result of the conversion of the metastable liquid to the crystalline compound. This embryo is bounded by a surface which has a positive free energy, Δf_s per unit area, associated with it. If the embryo grows above a "critical" radial size, Δf_v dominates and the embryo survives to nucleate, otherwise Δf_s dominates and the embryo disappears back into the melt, as shown in Figure 5 [8].

It follows from this simple picture that atomic mobility, stresses and strains within a solid, impurities, surfaces, and the composition difference between the background amorphous alloy and the embryo will affect the magnitude of the nucleation barrier preventing the crystallization of the amorphous intermediate. Unfortunately, there are few experimental results from which the importance of the

above effects can be estimated, due to the complexity of the reacting system and the lack of a suitable experimental probe.

The view of an interfacial reaction as a kinetic process is given support by the observation of a maximum experimental thickness for the amorphous phase formed. The formation of an amorphous interfacial layer between reacting solids is thought to result from competition between diffusion and nucleation [29]. Initially, as a result of the short diffusion path and high diffusion rate, the interface moves at a quicker rate than that for nucleation of a crystalline compound at the interface. Thus, the interface moves before a nucleus at the interface can reach its critical size. As the thickness of the amorphous alloy increases, the rate of movement of the interface decreases. At some critical thickness of the amorphous phase, the rate of interfacial movement will become comparable to the nucleation rate and at that point the amorphous phase will crystallize.

2.4. The Mechanism of a Solid State Reaction

The results obtained in the three diffusion length regimes discussed are consistent with the following picture of the evolution of a bulk binary diffusion couple. As two elements react, the local composition gradient is reduced as interdiffusion broadens the interface. The interfacial region expands with time, as long as enough energy is supplied to overcome the activation barrier for diffusion. Eventually, the compound with the smallest nucleation barrier crystallizes at the interface. The composition of the amorphous phase formed at the interface has a major influence on the activation barriers for nucleating different compounds. Nucleation of a crystalline compound is controlled by kinetics, as the phase which nucleates depends on an activation barrier and not the final free energy. Because growth of this phase within the interdiffused, amorphous interface involves only a local rearrangement, it does not depend on long-range diffusion. Therefore, the new phase initially can grow at a rate exceeding the bulk diffusion rate as it consumes the amorphous interfacial region and reestablishes steep concentration gradients at the compound/element interfaces.

Further growth of product depends on transport of the elements through the intervening compound layer, that is, on long range diffusion. As the thickness of this product layer increases, the diffusion path of reactants increases, and the growth rate of the new phase slows. As a consequence, the concentration gradient at both product/element interfaces again decreases. A second nucleation process can then occur at these developing interfaces in which another crystalline compound forms. This process continues until there is a distribution of compounds characteristic of the bulk diffusion couple.

A thin-film diffusion couple differs from a bulk diffusion couple in that the supply of one of the elemental reactants is exhausted before the nucleation of a second crystalline compound. On further heating, the remaining compound/element interface develops an amorphous interfacial phase which subsequently crystallizes. This second compound then grows until it exhausts the initially crystallized compound

or the remaining element. This process repeats until the final equilibrium distribution of products is obtained.

The rate-limiting step in thin-film diffusion couples is nucleation. We define thin-film diffusion couples as those which exhibit this sequential evolution of compounds. The thickness of the elemental layers at which this change in behavior occurs is determined by the relative size of the interdiffusion coefficients and the barriers for the nucleation of various compounds in the phase diagram.

An extension of the above discussion suggests that by further reducing the length scale of a diffusion couple, a diffusion-distance regime could be reached where all nucleation is suppressed. Nucleation preferentially occurs at interfaces as a result of concentration gradients, stresses, and strains. If an interfacial region must attain a certain width before a compound can nucleate, there must be a second critical length scale below which a layered system will interdiffuse completely without nucleating any crystalline products. This occurs because the interface, which is associated with a lower nucleation barrier due to its stresses and strains, will diffuse away before a nucleus of critical radius has had time to form. This second critical distance will depend upon the relative sizes of the activation barrier for nucleation both at the interface and in the homogeneous, amorphous alloy as well as the activation barrier for diffusion. We refer to systems layered below this second critical distance as ultrathin. A special case of this length scale regime is a solid state amorphization reaction in which the critical distance is hundreds of ångstroms.

3. SYNTHETIC STRATEGY

3.1. General Considerations

The ideal synthetic approach to a desired compound involves the rational choice of specific reaction conditions and steps designed to prepare the final compound as selectively as possible (i.e., with the highest yield). In an ideal synthesis, minor modifications of the reaction steps should permit the necessary flexibility to prepare any one of a family of products, regardless of their absolute thermodynamic stability. This type of a synthetic approach is necessarily based on controlling the kinetics of individual reaction steps, which permits the synthesis of kinetically (rather than thermodynamically) stable products.

The key to applying this general philosophy to solid state synthesis is identifying and controlling a kinetic step in the reaction mechanism. As mentioned previously, a solid state reaction consists of two key steps, interdiffusion of reactants and nucleation of products. Most synthetic approaches to solid state materials are diffusion limited, resulting in the most thermodynamically stable products. Any attempt to gain complete, kinetic control of the reaction pathway must be based upon eliminating diffusion as a rate-limiting step. This can be accomplished by

using a homogeneous, amorphous state as a reaction intermediate for the preparation of extended solids.

The utility of using a homogeneous, amorphous state as the reaction intermediate, permitting the separation of long-range diffusion from nucleation, has long been recognized. Extensive investigations have shown that use of solutions, melts, glasses, and gels as reaction intermediates provides access to the formation of metastable crystalline products [30–35]. Each of these techniques involves intimate mixing of the components; therefore, long-range diffusion of atoms or ions is not necessary. Crystalline products can be formed at much lower temperatures than those required to overcome diffusion in traditional solid state reactions. These methods have yielded metastable phases which are difficult or impossible to prepare by traditional high-temperature methods. However, the complex chemistry associated with these techniques has limited their generality. In addition, these techniques do not allow the controlled synthesis of a particular structure and therefore must be used in an empirical manner.

The use of intimate mixing combined with diffusional control is used to limit and direct reaction pathways and control intermediates via a very clever "soft chemistry" approach [31,36,37]. This approach takes advantage of large differences in diffusion rates often found in low-dimensional solid state compounds. For example, the oxide $K_2Ti_4O_9$ consists of two-dimensional sheets of titanium octahedra sharing edges and faces. These sheets are separated by K^+ cations, which are much more mobile than the Ti^{4+} cations. Washing the $K_2Ti_4O_9$ in acid results in the formation of the cation-exchanged material $H_2Ti_4O_9$. This phase evolves water on heating, causing the sheets to fuse together via the elimination of a specific oxygen atom, the most acidic one, in the layered structure. The resulting solid obtained via this "chimie douce" approach is a new metastable form of TiO_2 [38]. This approach, although extremely elegant, is limited by the availability of suitable precursor solids.

What is required to overcome the limitations of the above techniques is a generally accessible, intimately mixed, metastable reaction intermediate. The simplest intimately mixed system is one which contains only the elements of the final structure. In most cases, such a homogeneous noncrystalline system is a solid at room temperature and is commonly referred to as an amorphous alloy. Such an alloy, although containing the components of a solid state reaction, stands in sharp contrast to the heterogeneous, diffusion-limited systems typically found in most solid state reactions. Long-range diffusion is completed in the formation of the alloy. This leaves nucleation as the rate-limiting step in the formation of an extended solid.

Nucleation is an important phenomenon in many areas of chemistry and materials science. It has been extensively explored by the glass community, which has shown that nucleation of a crystalline solid from an oxide glass can be controlled by several strategies, such as incorporating impurities which act as nucleation seeds, using crystalline substrates as templates for nucleation, and changing such basic chemical parameters as composition of the glass. The formation of a glass

ceramic is an elegant example of the ability to control nucleation [39]. Diffusion control can also be used to limit the reorganization possible in crystallization by limiting the reaction temperature. A primitive example of this is the ability to control the crystallite number and size by controlling annealing temperature and time. Many of these concepts should also be applicable to the crystallization of other, non-oxide amorphous materials.

Although the amorphous state has several very attractive features as a reaction intermediate, its general use has been limited by the inability to isolate bulk amorphous material. Routes to amorphous alloys include the rapid cooling of molten alloys, referred to as splat cooling or melt spinning, codeposition of the respective elements, and low-temperature solid state amorphization reactions [40,41]. All these techniques are based on limiting the opportunities for the system to nucleate. The important energies in this situation are those required for nucleation and diffusion. Time is also important, as local rearrangements to form nuclei are limited by the diffusion rates.

Each of these techniques has drawbacks for the general preparation of amorphous alloys. Amorphous phase formation by rapid quenching of a high-temperature liquid is complicated by the importance of experimental variables [42]. The structure, for example, depends upon the local quench rate. Differences in structure can be seen between the two surfaces of a melt-spun ribbon, only one side of which quenches in contact with the cooling wheel. In codeposition, the structure of the amorphous alloy formed depends on deposition rates and the temperature of the substrate during the deposition process. These experimental parameters affect the surface diffusion pathlength during the codeposition. The critical experimental parameters limiting the ability to form amorphous alloys via ultrathin-film reactions are the individual layer thicknesses, temperature, annealing, and time.

Another major drawback of these techniques is the limited range of stoichiometries which can be prepared [43]. This curtails their synthetic utility. Various researchers have attempted to correlate size mismatch between the elements forming the alloy, diffusion rates, the relative structural stability of the amorphous alloys with respect to equilibrium compounds, and the heat of mixing with the extent of composition for which an amorphous alloy can be prepared [44–50]. There is no general consensus. Our opinion is that this is not a fundamental problem but an experimental one. As the ability to quench a sample faster has developed, the range of amorphous alloys which can be prepared has expanded. If a technique to prepare amorphous alloys over a greater compositional range can be developed, the use of these alloys as general synthetic intermediates would be enhanced.

3.2. Synthetic Approach

After surveying the literature presented as background in this chapter, we decided that superlattices presented several unique properties which could be exploited for their use as initial reactants. The two most important characteristics of superlattices

are the ability to tailor their structure on an ångstom length scale and monitor changes in their structure via X-ray diffraction. The ability to control diffusion length by varying layer thickness permits direct control of diffusion time and indirectly permits the defect densities responsible for low-temperature diffusion to be controlled. The diffraction pattern resulting from the regular, layered nature of superlattices offers the possibility of conducting detailed studies into the mechanism of solid state reactions. The ability to study the interfacial reactivity of these multilayers and the effect of initial structure on reaction kinetics is unique and allows a rational approach to making the desired amorphous intermediates.

Available information concerning the evolution of diffusion couples of varying length scale supported our decision, suggesting that low-temperature interdiffusion of superlattice composites was the best option available for preparing amorphous alloys as unique reaction intermediates. We deduced from the available experimental data that by preparing superlattices modulated on a short enough length scale, an amorphous intermediate could be prepared in most if not all systems. Our second choice of a general route to an amorphous intermediate was codeposition of the elements. We decided that the diffusionally constrained nature of the sequential deposition of layers followed by a low-temperature anneal to an amorphous alloy was a potentially important distinction between sequential deposition and codeposition. In sequential deposition, only one element has significant mobility at a time. During codeposition all the elements within the alloy have similar diffusional freedom and high surface diffusion rates.

Finally, we also thought that the diffraction patterns resulting from a superlattice were uniquely suited for studying the earliest stages of a solid state reaction. It is known that monitoring the decay of superlattice diffraction patterns with time at a particular temperature is the most sensitive technique available to quantify diffusion rates. Diffusion rates as small as 10^{-25} cm^2/sec have been measured via this technique. Since the intensities of the diffraction peaks result from the structure of the repeat unit, monitoring the intensities of all the observable diffraction peaks as a function of annealing temperature and time would, in principle, permit changes in interfacial structure to be observed on an ångstom length scale.

Presently, little is known about the earliest stages of solid state reactions—before the formation of a crystalline product at the interface [51]. Considering the difficulty of the experiment this is not surprising. The interfaces of a bulk diffusion couple make up only a minute fraction of the sample, and such buried interfaces are difficult to observe. Superlattice reactants can be modulated on a fine enough length scale that they consist almost entirely of interfaces. Studying the initial solid state reactions occurring in superlattices via changes in the superlattice diffraction patterns potentially can provide important information regarding the initial steps of bulk solid state reactions.

The overall scope of these studies is to prepare initially layered composites in which the reactants interdiffuse to form a homogeneous, amorphous alloy. The structure of the initial composite, the layering sequence and layer thicknesses, is tailored to facilitate this pathway. The structure of the as-deposited films provides

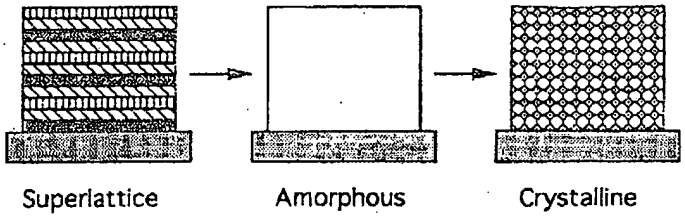

Figure 6. Thermal evolution of an ultrathin-film superlattice.

a well-defined synthetic starting point and parameters which can be correlated with subsequent reactivity. The rate-limiting step in forming a crystalline compound via this reaction mechanism is nucleation. The desired reaction pathway for such a general ultrathin-film composite is shown in Figure 6.

4. PREPARATION OF SUPERLATTICES

The first experimental step in studying the proposed reaction mechanism is developing the ability to prepare superlattice composites modulated on an ångstrom length scale. Superlattices are most commonly produced by the sequential deposition of elemental layers in a high vacuum environment [52,53]. The design of a deposition system to make superlattice reactants must permit any sequence of individual elemental layers to be deposited, allow for the independent control of the individual layer thicknesses, and also produce a usable quantity (1–10 mg) of superlattice materials for subsequent study.

The ability to deposit any sequence of layers and the independent control of layer thicknesses are crucial for both understanding and controlling interdiffusion reactions, as they permit the creation of complex layer sequences designed to control the diffusion process. As a simple example, the reaction of a composite based upon the repetition of the layer sequence ABC involves the simultaneous reaction at AB, BC, and AC interfaces while the reaction of a composite based upon the repetition of the layer sequence ABCB involves initial reaction of only AB and BC interfaces. Thus, the repeat unit of a superlattice composite can be used as an experimental variable to investigate and control solid state reactions.

The deposition system used to prepare the samples in our investigations, shown schematically in Figure 7, has fixed deposition sources, a set of computer-controlled shutters, and a movable sample stage. The configuration of these components within the deposition chamber is shown in Figure 8. The deposition system is computer controlled and monitored, as shown via the electrical block diagram of Figure 9, thus permitting a tremendous amount of flexibility in preparing samples. All the monitoring signals during the layering of a sample are saved on the computer as a function of time, providing a detailed history for each sample [54].

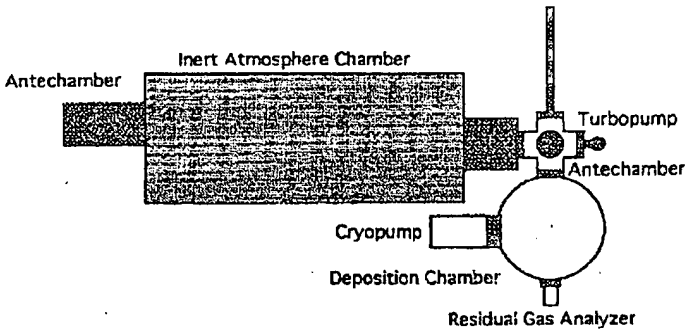

Figure 7. Schematic top view of the deposition system used at the University of Oregon to prepare superlattices.

The operation of the deposition system is simple. Each of the sources used in the deposition process is simultaneously brought up to the desired deposition rate and stabilized. A sample is moved above source A and the shutter is opened. When the desired amount of A has been deposited (as indicated by a deposition monitor), the shutter is closed and the sample is moved to the next source, B. When the desired amount of B has been deposited, the sample is moved over the next source (either A or another element) and the process continued until the repeat unit is constructed. The sample movements and shutter operations are then repeated until the desired number of repeat units have been deposited, completing the superlattice.

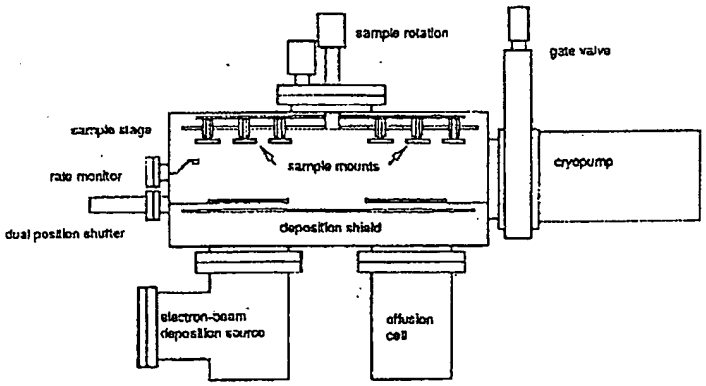

Figure 8. Schematic of the internal arrangement of deposition sources, shutters, and samples in the deposition chamber.

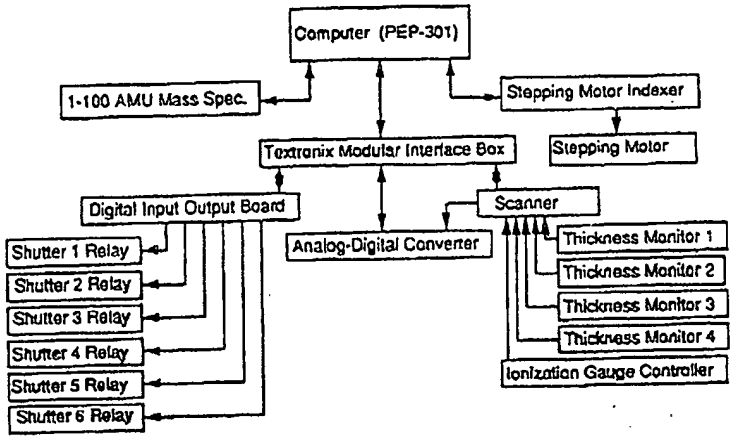

Figure 9. Block diagram of the electronics associated with the deposition chamber.

A knowledge of constituents responsible for the background pressure is important, since the impurity level of a layered reactant is a function of the background gases' partial pressures as well as the impurity level of the source material. Background pressures vary considerably depending on the elements being deposited. The partial pressures of background gases are monitored using a residual gas analyzer with a mass range of 1 to 104 amu. The kinetic theory of gases can be used to estimate the worst case impurity levels in a sample from the residual gas pressures and deposition rate. For a background pressure during deposition of 5×10^{-8} torr, the major gas species during the deposition process is hydrogen, typically at a pressure of 3×10^{-6} torr. The gas species with the next highest partial pressure is water at a pressure of 1×10^{-6} torr. For deposition rates of 1Å/sec, and assuming a sticking coefficient of 1 for water molecules hitting the superlattice surface (a worst case example), the purity of a deposited sample is 99.5% with respect to oxygen. This impurity level is comparable with the available atomic purities of many of the elemental sources.

An important problem discovered during the preparation of samples lies in the variation of the proportionality factor between the layer thicknesses reported by the deposition monitors and the measured repeat distances found in the superlattices. We employ quartz crystal monitors to control deposition rates and monitor the amount of an element deposited in a layer. These monitors work by measuring the frequency shift of a driven oscillating quartz crystal as mass is deposited on the surface of the crystal. This frequency shift depends on such physical properties of the element being deposited as mass, density, and shear modulus. The proportionality factor converts the frequency shift into a mass and is determined from a

sequence of calibrations. We have found that this proportionality factor can change significantly during the course of a series of depositions, degrading the ability to control the stoichiometry of the superlattices produced.

The variability of the proportionality factor arises from changes in the acoustical impedance of the deposited layer during a sequence of depositions. The first change in acoustical impedance occurs when the initially amorphous element crystallizes upon the quartz crystal. This change in acoustical impedance can be experimentally avoided by predepositing several hundred ångstroms of an element upon the crystal monitor. The second change in acoustical impedance occurs if a crystal upon which an oxidizable metal has been deposited is exposed to air. Subsequent deposition upon that crystal will have a different frequency shift than the original deposition.

We have found that to obtain reproducible and accurate sample stoichiometries, each of the oscillator crystals must be dedicated to a single element. Further improvement in crystal accuracy can be obtained by using new crystals for each deposition cycle. A plot of the intended versus measured layer thicknesses is used as a measure of the accuracy of the crystal monitors, and deviations of less than 2% can be realized.

5. CHARACTERIZATION OF SUPERLATTICES

Following the preparation of a superlattice reactant, it is important to confirm the layered structure of the initial reactant and the layer spacing. We characterize the deposited superlattices via several techniques which are discussed in detail in the following sections. Our main analytical tool is low-angle X-ray diffraction. This technique permits us to determine the size of the repeating layer sequence, the abruptness of the interfaces in the superlattice, and the coherency of the layering. The topography of the superlattices is investigated using both scanning electron microscopy and scanning tunneling microscopy. The impurity levels are investigated using Auger spectroscopy. Composition is determined via X-ray diffraction techniques, atomic absorption, and nuclear activation analysis. The layered nature of the superlattices and their composition have been confirmed using depth profiling secondary ion mass spectroscopy. The presence of any crystalline compounds in the initially layered composites is determined by high-angle X-ray diffraction. Following a discussion of the application of these techniques to our superlattices, a descriptive summary of a typical superlattice structure will be presented.

5.1. Low-Angle X-Ray Diffraction

The low-angle diffraction pattern observed for a superlattice results from the artificial layering produced in the sample as it is prepared. It is not due to crystallinity in the normal sense of exact positions for each atom in the unit cell. Rather, the diffraction signal results from the modulation of the electron density

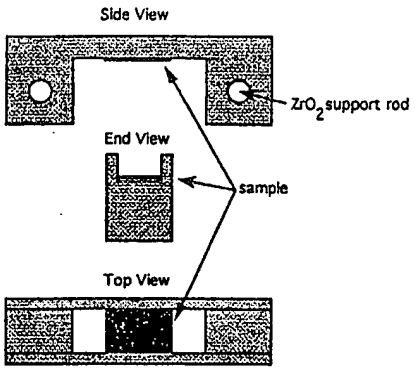

Figure 10. Schematic of sample stage used for low-angle diffraction experiments.

due to the regular repeat of elemental layers. The intensity of the diffraction signals reflects the electron density distribution within the composite.

Since the superlattices are artificial single crystals in the direction perpendicular to the substrate, the diffraction intensities are very dependent on alignment. This sensitivity to alignment is the main experimental concern when examining super-

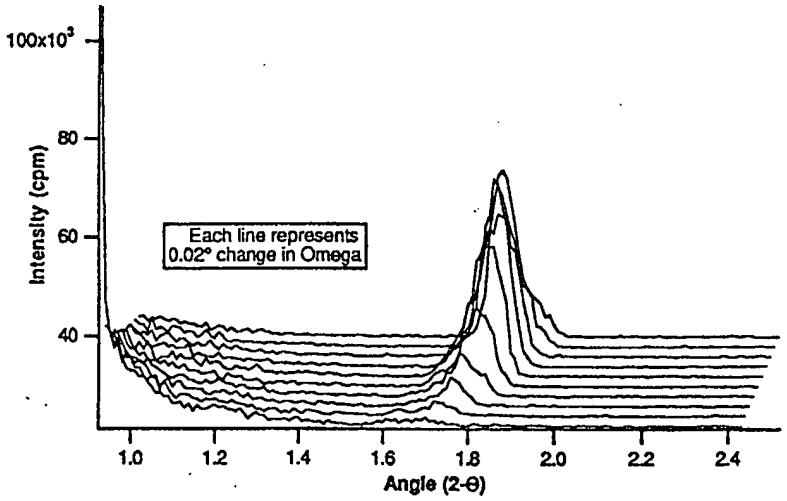

Figure 11. Intensity of a second-order low-angle superlattice Bragg reflection in theta-omega space, illustrating the importance of angular alignment. The change in the intensity and position of the first-order reflection is much larger and would be off scale in this figure.

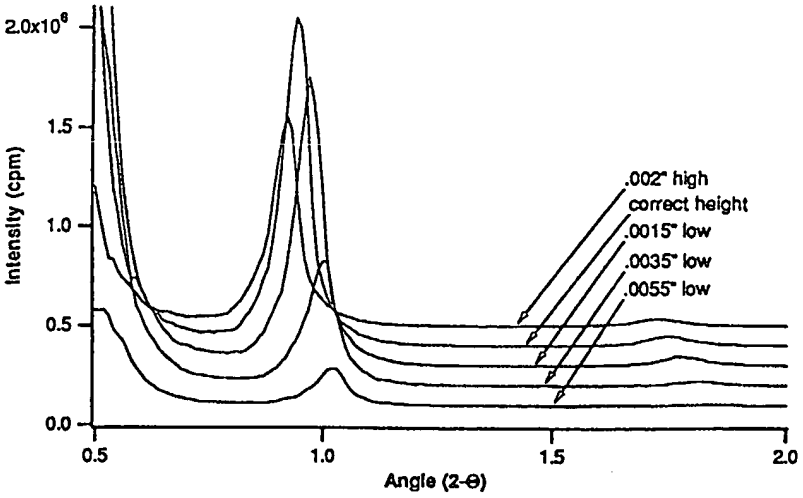

Figure 12. Effect of sample height on the intensity and position of a low-angle superlattice Bragg reflection.

lattices with diffraction techniques. The design of the custom sample stage used in our laboratory is illustrated in Figure 10. The sample stage consists of a pair of machined optical flats upon which the sample is held by a spring steel clip. This stage is positioned off a standard conflat high-vacuum flange by two quarter-inch ceramic rods. The conflat mounting flange is attached to a vertical positioning stage with a 0.0001 in. micrometer adjust which permits the height of the sample stage to be varied in a reproducible fashion. This sample stage permits rapid alignment. Diffraction scans remain constant with the removal and reinsertion of a sample.

The above sample stage was used to probe the sensitivity of intensity and position of the low-angle Bragg diffraction peaks to sample alignment in a theta-theta diffraction geometry. Figure 11 illustrates that the diffraction angles must remain within 0.005 of a degree of alignment to obtain true intensity information. Figure 12 shows the effect of changing the sample height on diffraction intensities and positions for a representative multilayer composite. This illustrates that the sample height must be within 0.001 in. to obtain true intensity and position information of the Bragg diffraction profiles.

Figure 13 contains a representative diffraction pattern of a superlattice prepared in our laboratory. The intended structure of this superlattice consists of ten identical layers, each containing 22±1Å of silicon and 44±1Å of iron. This low-angle diffraction pattern clearly contains several intense Bragg reflections resulting from the structure of the superlattice as well as subsidiary maxima between these Bragg reflections.

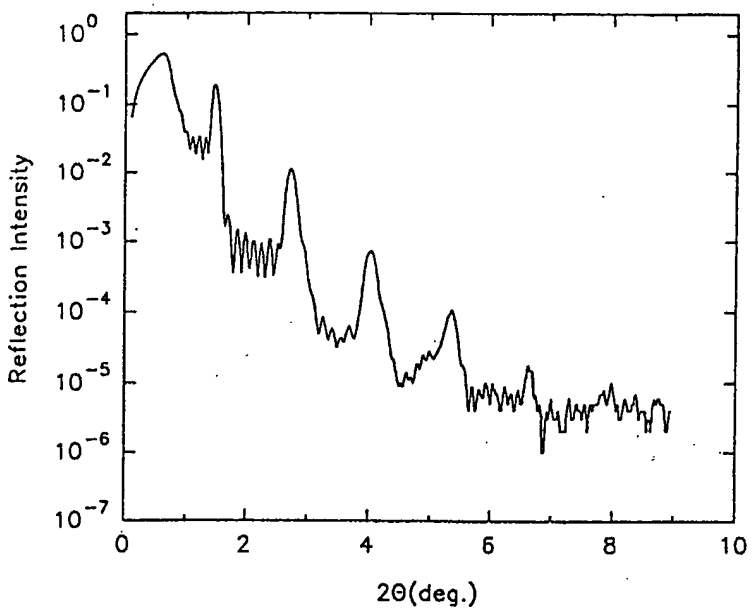

Figure 13. Representative diffraction pattern of a superlattice. The intended structure consists of ten identical layers, each containing 22 ±1 Å of silicon and 44 ±1 Å of iron.

Data Analysis

The analysis of the diffraction intensities from superlattices to yield structural information has been the subject of over 50 papers in the last ten years [55–78]. The approach used in most of these papers is to develop a model superlattice and then calculate the diffraction intensities as a function of angle.

The goal of our efforts in this area was to develop data analysis techniques to separate and extract realistic structural information. The positions, widths, and intensities of diffraction signals resulting from a multilayer depend intimately on the structure of the superlattice. The parameters describing the structure of a superlattice can be roughly divided into four categories:

1. the average thickness of each of the individually deposited elemental layers;
2. the topographical characteristics of the substrate and the surfaces of the subsequently deposited layers;
3. the extent of interdiffusion between the deposited layers occurring during the deposition; and
4. the coherence/incoherence of the topography and interdiffusion occurring at each interface.

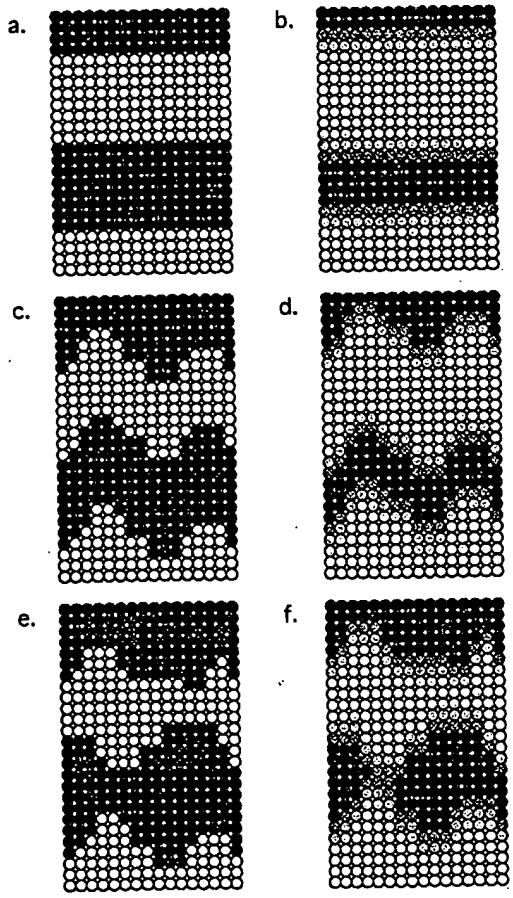

Figure 14. Schematic illustration of structural parameters influencing the intensity of low-angle diffraction patterns. **a.** Coherent superlattice with smooth, abrupt interfaces; **b.** Coherent superlattice with smooth but diffuse interfaces (shading is used to indicate percent site occupancy of A and B); **c.** Coherent superlattice with rough interfaces; **d.** Coherent superlattice with rough, interdiffuse interfaces; **e.** Incoherent superlattice resulting from incoherent roughness at the A–B interface; **f.** Incoherent superlattice with interdiffuse, incoherent, rough A–B interfaces.

These characteristics are illustrated in Figure 14.

The simplest characteristic of the diffraction pattern of a superlattice is the position of the Bragg diffraction maxima. As in conventional crystallography, the position of these maxima are determined by the size of the unit cell. In a superlattice, this consists of the sum of the thicknesses of the individual elemental layers within the repeating unit. To a first approximation, the positions of the Bragg maxima are given by the Bragg equation,

$$2d\sin(\theta) = n\lambda, \tag{1}$$

where d is the size of the repeat distance within the superlattice, λ is the wavelength of the incident X-rays, and θ is the angle of incidence between the X-ray beam and the surface of the superlattice.

There is a significant correction to Equation (1) at low angles due to a change in refractive index at the surface of the superlattice [79]. This causes the angle of the incident X-rays to change at the interface, resulting in a discrepancy in the position of experimental diffraction maxima from that calculated using Bragg's law. This correction to Bragg's equation, derived for a uniform thin film, is given by

$$2d_{true}\left[1-\frac{\delta}{\sin^2(\theta)}\right]\sin(\theta) = n\lambda, \tag{2}$$

where δ is the index of refraction of the film. A weighted average value for the index of refraction, valid when the repeating unit of the superlattice is thin, is used when applying this equation to the diffraction pattern of a superlattice. This expression can be rearranged to yield

$$\frac{1}{d_{obs}} = \frac{1}{d_{true}} + \frac{2\delta}{n\lambda\sin(\theta)}, \tag{3}$$

where d_{obs} is defined by Equation (1). A plot of $1/d_{obs}$ versus $1/\sin(\theta)$ for the observed diffraction orders should yield a straight line, the slope of which is proportional to an effective index of refraction for the multilayer and the intercept of which is $1/d_{true}$. The deviation from linearity of this plot is used to determine an associated error for d_{true}. For the majority of the multilayers prepared in our laboratory, the error associated with the size of the repeat unit is the larger of 2% of the repeating unit or 1 Å.

While the positions of the diffraction peaks depend on the size of the unit cell, the experimental intensities are determined by the contents of the repeat unit and the consistency and coherency of the contents between repeat units. The experimental intensity data collected in a theta-theta or theta-two-theta manner must be corrected to compensate for the change in the volume of sample probed as a function of incident angle. If the incident beam is assumed to penetrate to the bottom of the multilayer, a simple geometric argument shows that the volume of sample illuminated is proportional to $1/\sin(\theta)$. To normalize experimental data to constant volume, the experimental intensities must be multiplied by $\sin(\theta)$.

ng the intensity of
abrupt interfaces;
is used to indicate
ough interfaces;
crent superlattice
crent superlattice

The difficulty in analyzing intensity data of superlattice reflections results from the fundamental difference between superlattices and naturally occurring crystals. The variation in the size of a unit cell in a natural crystal (excepting the small percentage of cells with defects) is on the order of 0.001Å and the atoms are located in specific positions. In a superlattice, the unit cell size varies on an ångstrom scale, there can be significant incoherence between the topography of the substrate and subsequently deposited layers, and the interdiffusion at the interfaces potentially can vary from layer to layer. Thus, the traditional crystallographic models used for natural crystals need to be corrected for these experimental limitations.

More insight as to the origin of these experimental limitations can be gained by examining the growth process involved in preparing a multilayer by evaporation in high vacuum. The deposition substrate is not atomically flat but has hills and valleys on a large scale (hundreds of ångstroms) in addition to sharper features on an ångstrom scale. The height of these features varies with the substrate. Sample preparation begins by depositing the first element (A) upon the substrate at approximately 1 Å/sec. At this deposition rate, 10^{15} atoms/sec are hitting each square centimeter of substrate surface. The A atoms can react with the substrate. The depositing element can coat the substrate evenly, fill in the valleys preferentially, and/or cluster into islands during deposition. During the deposition of the second element (B) the same questions need to be addressed. In general the A/B and B/A interfaces will be different, caused by the different reactivities of the depositing A atoms onto B and B atoms onto A. Since the methods used to control the layer thicknesses are only accurate to approximately an ångstom, there will be variations in the average layer thicknesses. In addition to this variation in the average layer thickness, there can be larger local variation of layer thicknesses throughout the multilayer due to islanding during growth. These local variations can arrange coherently between layers or be spatially incoherent.

Two approaches, a kinematic theory of X-ray scattering and a dynamical theory, have been used to calculate the diffraction intensities obtained from the actual complex structure of a multilayer. In a kinematic approach, it is assumed that the thickness of the multilayer is small, such that each of the interfaces is exposed to the same incident intensity. This is the approximation typically made in the structure determination of small molecules by X-ray crystallography. In a dynamical approach, the intensity of the incident X-rays is calculated as a function of penetration depth, since for the strongest reflections, an appreciable fraction of the incident beam can be reflected at each interface. Thus, an interface deep within a multilayer will see a smaller incident intensity than one near the surface.

In both the kinematic and dynamic approaches, the complex structure of a multilayer is typically approximated by an ideal, perfectly regular, and coherent one-dimensional superlattice. Results obtained on this ideal, simplified system are then modified by correction terms to take into account the complexity of the "real" system. The formulation of the kinematic approach easily incorporates a diffuse interface and has been used to model interdiffusion. The analysis of diffraction data from superlattices in the soft X-ray regime, where higher reflectivities can be

obtained, has been dominated by a dynamical reflection/transmission model, in which the superlattice structure is assumed to consist of repeating units of perfectly flat, alternating layers of high- and low-electron-density elements with abrupt interfaces. The optical properties of the elements are then used to calculate the interference pattern resulting from X-rays impinging upon the multilayer.

Our analysis of the Bragg intensities from superlattices has evolved from a kinematic to a dynamical approach. The kinematic approach was initially used because a significant amount of interdiffusion occurs during deposition, caused by the reactive combinations of elements used in our experiments. The interdiffused nature of the interfaces is particularly easy to introduce into a kinematic description of the diffraction of a superlattice. This approach also facilitated the separation of coherent effects (such as diffusion of the elements at the interfaces) from incoherent effects (such as interfacial roughness). When including incoherency in the model, we switched to a dynamical reflection/transmission model using a recursive method.

Diffraction from Perfectly Coherent Superlattices

A perfectly coherent superlattice consists of alternate layers of light and heavy elements which are exactly repeated to form each unit cell. Each of the A (and also B) layers in an ideal A–B multilayer have identical thicknesses and composition profiles at the interfaces. The diffraction pattern results from the modulation of the electron density. The simplest interfacial composition profile is atomically abrupt and perfectly smooth, and is the one most commonly used to describe and predict the intensities of the Bragg diffraction maxima from superlattices. Either the kinematic or dynamical approach can be easily applied to calculate the intensities of Bragg reflections for this simple structural model of a superlattice. In the discussion which follows, the kinematic approach is developed and then used to calculate the diffraction profile of perfectly coherent superlattices.

The relative intensities of Bragg diffraction maxima are determined by the electron density distributions within the unit cell. The peak widths, positions, and relative intensities of the various diffraction peaks are given by

$$I_n = A_n^2, \tag{4}$$

where

$$A_n = \left[\frac{\sin(\pi N d \cdot s)}{\sin(\pi d \cdot s)}\right] \int_{z=0}^{1} P(z)\cos(2\pi \cdot z)dz \tag{5}$$

or

$$A_n = \left[\frac{\sin(\pi N d \cdot s)}{\sin(\pi d \cdot s)}\right] F_s. \tag{6}$$

a. Main maximum:
d·k=0

b. First minimum:
d·k=1/4

c. First subsidiary maximum:
d·k=3/8

d. Second minimum:
d·k=1/2

e. Second subsidiary maximum:
d·k=5/8

f. Third minimum:
d·k=3/4

g. Main maximum:
d·k=1

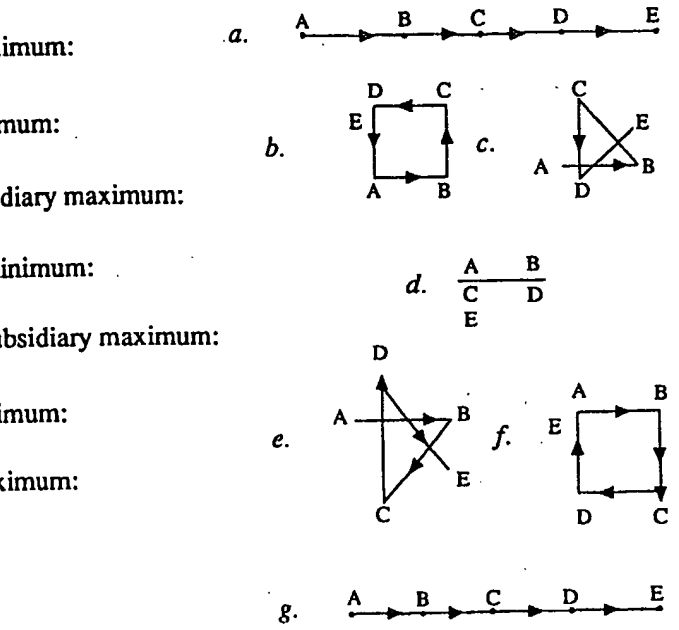

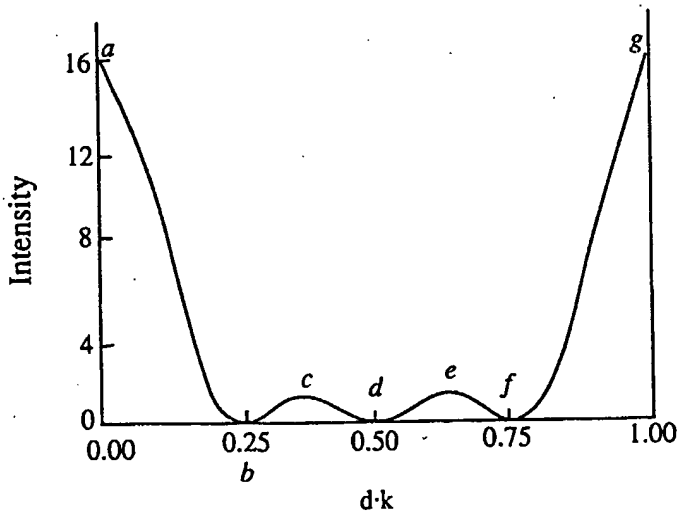

Figure 15. Phase vector diagram showing the formation of maxima and minima of intensity for a four repeat unit multilayer.

In Equations (4)–(6), I_n is the diffraction intensity of the nth order Bragg peak, d is the repeat unit in the composite, s is the scattering vector, N is the number of repeat units in the superlattice, z is a reduced coordinate, and $P(z)$ is the electron density distribution through the unit cell. The first term in Equation (6) gives the position and line width of the diffraction maxima while the second term, F_s, gives the relative intensity of the diffraction peaks.

This model yields primary maxima, called Bragg diffraction peaks, which arise from the completely in-phase scattering of X-rays off each of the superlattice interfaces. Subsidiary maxima also occur, resulting from the incomplete destructive interference of X-rays scattering off a small number of interfaces. The difference between the diffraction phenomena resulting in subsidiary maxima and Bragg reflections is more obvious when the diffraction events are represented by a phase vector diagram. A phase vector diagram containing the maxima and minima special points resulting from a four-layer superlattice is shown in Figure 15.

The intensities of the Bragg peaks are directly related to the magnitude of the F_s term, which is determined by the distribution of electron density within the repeat unit. Thus, the calculated diffraction pattern of a superlattice is very sensitive to the layer thicknesses of the elements making up the repeat unit and the composition profiles across the interfaces. Figure 16 contains diffraction patterns of several superlattices, calculated using Equation (5), illustrating the sensitivity of Bragg intensities to the thickness of the elemental layers making up the repeat unit. All the calculations were based on a ten-repeat-unit superlattice containing iron and silicon layers within the repeat unit, atomically abrupt interfaces, and a total repeat unit thickness of 67Å. This sensitivity to layer thickness can be used to confirm the layer spacings expected from the deposition process.

The second factor controlling the electron density distribution within the repeat unit is the concentration profile at the interfaces. To illustrate the effect of concentration profiles upon Bragg intensities, the diffraction pattern of a perfectly coherent superlattice made up of ten repeat units of 22.5 Å of silicon and 44.5 Å of iron with varying width interfaces is shown in Figure 17. The Bragg peaks as well as the subsidiary maxima remain in the same positions, but the intensities of the higher-order Bragg diffraction peaks rapidly attenuate as the interfacial width increases.

Although the above examples show the cause-and-effect relationship between diffraction intensity and electron density profile of the repeat unit, the determination of the electron density profile cannot proceed directly from the intensity measurements. The structural analysis is hampered by the inability to determine the phase of the structure factor. The mathematical relationship between the diffraction intensity and the electron density profile is given by Equation (5). We can take the Fourier transform of Equation (5) to produce an expression giving the electron density in terms of the Bragg diffraction intensities:

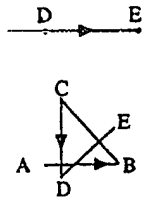

B
D

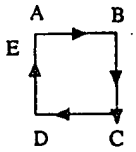

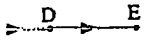

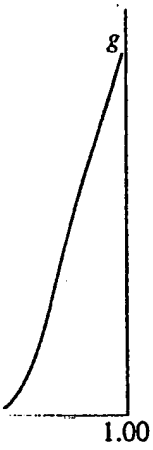

and minima of

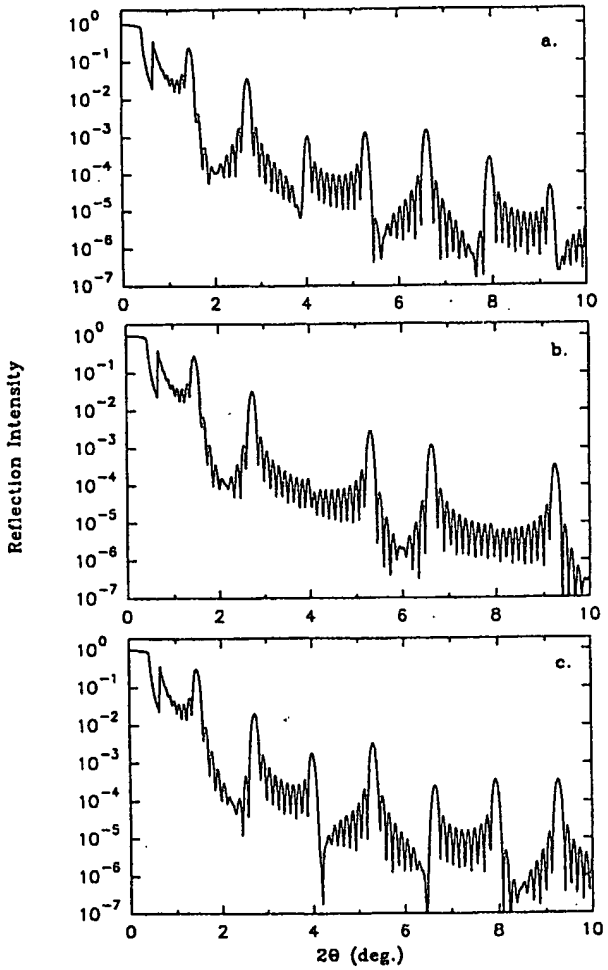

Figure 16. Calculated diffraction patterns of ten-layer superlattices consisting of 20 Å of silicon and 47 Å of iron (a), 22.5 Å of silicon and 44.5 Å of iron (b), and 25 Å of silicon and 42 Å of iron (c). The diffraction patterns contain both Bragg diffraction maxima and subsidiary maxima due to the incomplete destructive interference of the diffraction vectors originating from the interfaces. While the positions of the maxima remain constant, the relative intensities of the Bragg maxima change markedly.

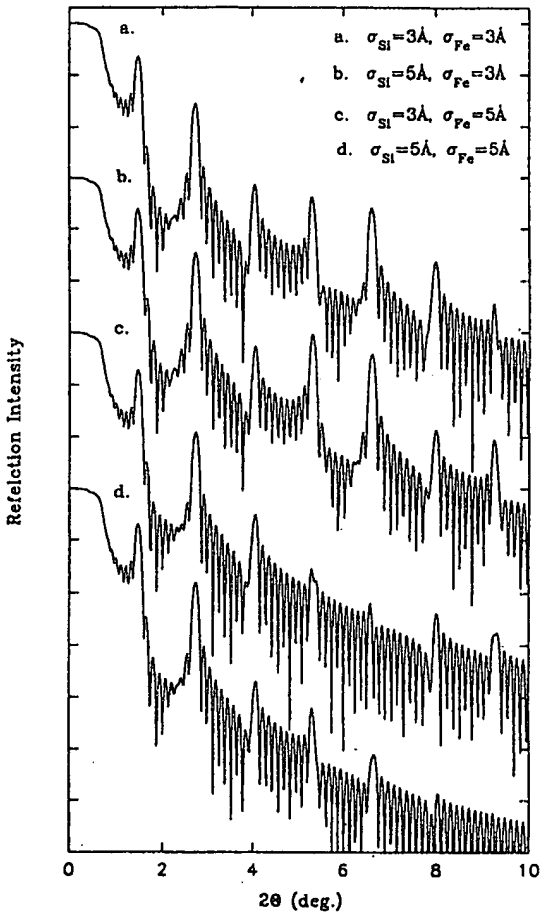

Figure 17. Calculated diffraction patterns of ten layer superlattices consisting of 22.5 Å of silicon and 44.5 Å of iron with varying electron density profiles at the interfaces due to interdiffusion. The interdiffusion profiles were calculated assuming Fick's law of diffusion. The diffraction patterns contain both Bragg diffraction maxima and subsidiary maxima due to the incomplete destructive interference of the diffraction vectors originating from the interfaces. While the positions of the maxima remain constant, the relative intensities of the higher order Bragg maxima are rapidly attenuated with interdiffusion.

$$P(z) = F_0 + B \sum_{n=1}^{\infty} F_n \cos(2\pi n z + j_n), \tag{7}$$

where j_n is a phase, F_n is the intensity of the nth diffraction order, and B is a scaling factor. Experimentally, the intensities of the diffraction peaks yield the modulus $|F_n|$, but the corresponding phase, j_n, is not directly measurable. This problem is the central difficulty in X-ray structure analysis [80,81].

The difficulty in determining the electron density profile within a repeat unit of a multilayer is compounded by the lack of criteria with respect to chemical reasonableness. In molecular structures, both bond distances and bond angles are used as objective criteria in determining the structure from the diffraction data. No such criteria exist for electron density profiles. The most common assumption is that the interface produced by depositing element A on top of element B is the same as that for depositing B on top of A. This assumption yields, for simple binary superlattices, a centrosymmetric repeat unit. Equation (7) then reduces to

$$P(z) = F_0 + B \sum_{n=1}^{\infty} (\pm) F_n \cos(2\pi n z), \tag{8}$$

where the phase problem is now reduced to determining whether to take the plus or minus square root of the intensity. One can use this relationship to derive an estimate of the interfacial widths by compiling the various possible sign combinations which yield the possible electron density distributions in the composite.

The ultimate goal in analyzing the superlattice diffraction data is to determine the average atomic concentrations of the elemental constituents as a function of position within the repeat unit. To accomplish this task, more information is required than can be obtained at a single X-ray wavelength. Since the atomic scattering factors are a function of the energy of the light used in the diffraction experiment, it is in principle possible to determine the distribution of atoms within the repeat unit by collecting Bragg intensity information as a function of energy [82].

Effect of Incoherence

Real superlattices contain several incoherent sources of variation in the electron density distribution. In a perfectly coherent superlattice all the incident X-ray flux is either reflected or transmitted. The effect of incoherency is to scatter or reflect a fraction of the incident X-rays at an angle different from that expected for an ideal superlattice.

The major sources of incoherence are local variations in thickness, deviations of an entire layer from the average repeat layer thickness, and variations in the topography of the interfaces due to variations in local interdiffusion and reaction during the deposition process. The effect of this incoherent "noise" upon the

diffraction signal depends on whether the signal is due to a Bragg reflection or a subsidiary maxima, and the magnitude of the correction to the coherent scattering varies with the diffraction angle.

We have explicitly included incoherent interfacial roughness by extending the Darwin–Prins dynamical theory to calculate the reflectivity of a multilayer having arbitrary interfacial profiles and with a variable degree of randomness in the interlayer spacing. This was accomplished by dividing the nonideal multilayer into a large number of thin slabs whose index of refraction was taken to be constant and that of the center of the slab. A recursion relationship was then used to calculate the reflection and transmission occurring at the interface of each slab. This calculation is done for a collection of layer thicknesses in which the deviation of each layer is chosen to be random within a given distribution width. The intensities as a function of angle are then added together and divided by the number to determine an average diffraction profile [83].

This approach is similar to the method of Warren and Averback for determining the domain size and degree of imperfection in ductile materials [84]. They divided a bulk crystal into an assemblage of domains which are slightly displaced from one another. The diffracted waves from each of these domains is incoherent and occur at slightly different angles. If the size of these domains is large with respect to the wavelength of X-rays, the intensities from a collection of domains can be added together to obtain the diffraction signal from the actual mosaic crystal. In the case of multilayers, adding the intensities obtained from a collection of perfect multilayers is an equivalent approximation if the domain size in the plane perpendicular to the layering is large compared with the coherence length of the diffracting radiation.

The effect of incoherent errors in individual layer thicknesses within a multilayer is shown in Figure 18. The diffraction signal obtained from a perfect multilayer is compared with those obtained from multilayers which have errors in individual layer thicknesses of varying magnitudes. The important conclusion from Figure 18 is that the incoherent errors have a much larger effect on the subsidiary maxima than upon the Bragg maxima.

In most samples produced in our laboratory, the largest sources of incoherence in the superlattices are deviations from the ideal layer thicknesses, roughness in the interfaces due to islanding of the elements during deposition, and variations in local interdiffusion during deposition. We have approximated these phenomena by adding together the calculated diffraction patterns of a collection of superlattices with various errors in their layer spacings. The results of these calculations are shown in Figure 19. The main result of local incoherence is to dramatically damp the subsidiary maxima due to the destructive interference of the scattering from various thickness domains. The angular position where the subsidiary maxima are no longer observed changes with the magnitude of the roughness, and this angular position can be used to estimate the roughness of the interface. This type of simulation agrees well with diffraction data from our samples, in which the subsidiary maxima disappear within a short angular distance.

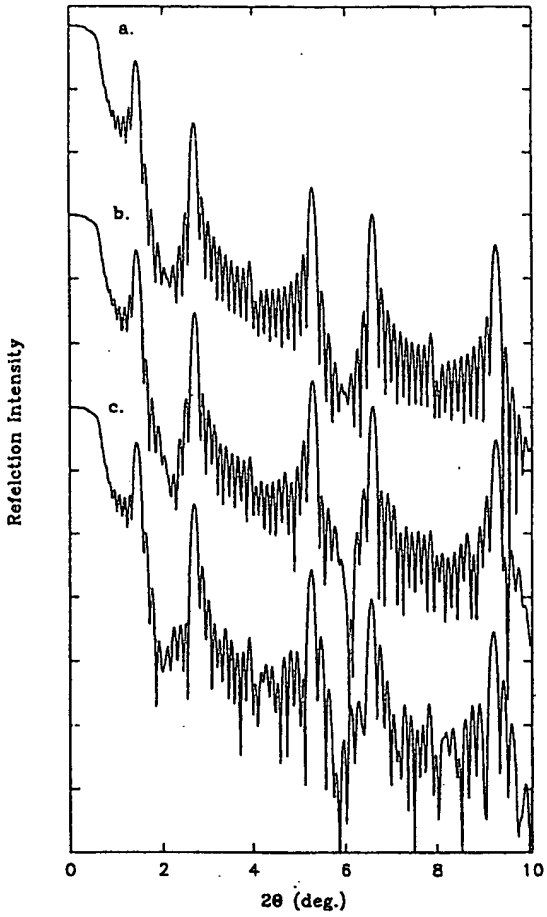

Figure 18. Comparison of the diffraction patterns obtained from a perfect superlattice (a), consisting of 22.5 Å of silicon and 44.5 Å of iron with abrupt interfaces between them, with superlattices containing an error in the thickness of either an individual layer (b), or several individual layers (c).

Summary

The diffraction pattern of a superlattice is a very sensitive probe of the quality of the layering and internal structure of the repeating unit. The size of the repeating unit of a superlattice is given by the peak positions. The number and intensity of the diffraction orders are indicative of the width of the interface within a repeat unit. The extent of incoherence within the superlattice can be estimated from the

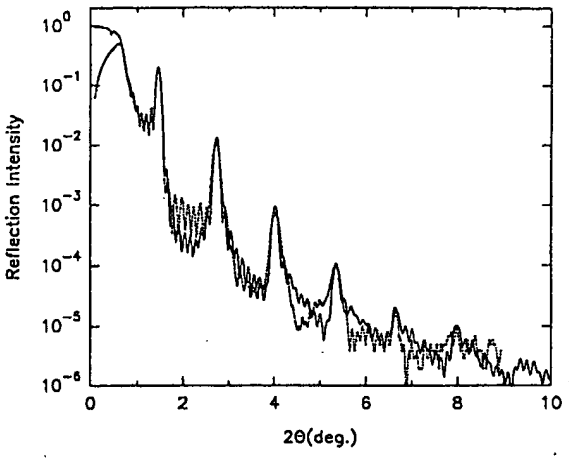

Figure 19. Plot of observed diffraction intensity for the iron silicon superlattice plotted in Figure 13 versus that calculated with a model including both coherent interdiffusion and incoherent local errors in the layer thicknesses.

intensity of the subsidiary maxima between the diffraction maxima. The quality of the layering in terms of deviations of individual layer thicknesses from the ideal can be estimated from the intensity variations of the subsidiary maxima. The agreement between the calculated spectrum and that observed for the iron–silicon superlattice shown in Figure 19 suggests that both coherent interdiffusion and incoherent roughness must be used to simulate the observed diffraction patterns.

5.2. Other Probes of Multilayer Structure

There are several other techniques which are commonly used to probe the structure of superlattices. These include high-resolution transmission electron microscopy, Rutherford backscattering, depth profiling secondary-ion mass spectrometry, scanning tunneling microscopy, and extended X-ray absorption fine structure. Results we have obtained using several of these techniques are discussed in more detail below.

Depth Profiling Secondary-Ion Mass Spectroscopy

In the depth profiling secondary-ion mass spectroscopy experiment, a beam of rare gas ions is accelerated into the surface of the sample which knocks atoms off the sample into the gas phase. The ions are then detected using a mass spectrometer. To maximize the depth resolution, the angle of the incident sputtering beam of argon atoms is kept as low as possible and the energy of the impinging beam is minimized.

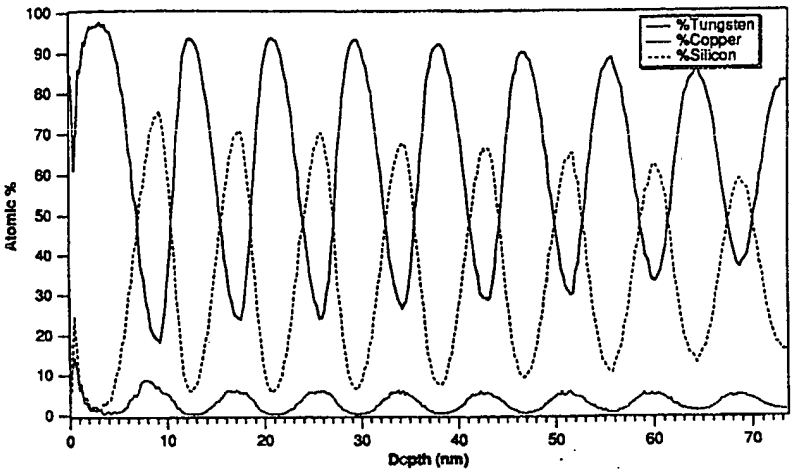

Figure 20. Depth profiling secondary-ion mass spectrometry data obtained on a Cu–Si–W superlattice.

A representative depth profile obtained for a Cu–Si–W composite under these conditions is shown in Figure 20. The modulated nature of the sample is readily apparent from the oscillating elemental signals as a function of sputtering depth. Further details of the compositional structure on a 10-Ångstom length scale; however, are difficult to obtain due to several experimental limitations. Primary among these difficulties is intermixing of the elements at interfaces as a result of the sputtering beam. This limits the depth resolution to approximately 10–20 Å. The asymmetry in composition profiles in Figure 20 is probably caused by differential sputtering efficiencies for the different elements. To confirm this, the sputtering experiment needs to be repeated from the backside of the sample and the profiles obtained from either direction have to be compared.

Scanning Tunneling Spectroscopy

Most of the analysis of superlattice diffraction patterns begin with the assumption that the sample is perfectly coherent and that the sample surface is smooth. We have used scanning tunneling spectroscopy to probe the surface structure of many of our samples. In general, we have found that surfaces of superlattices have a vertical roughness of 5–25Å over a surface area of 100 × 100 angstroms. We have found that details of the surface structure depend intimately upon the elements being deposited.

High-Resolution Transmission Electron Microscopy

High-resolution transmission electron microscopy has historically been the most used experimental tool to characterize the layer quality and crystallographic

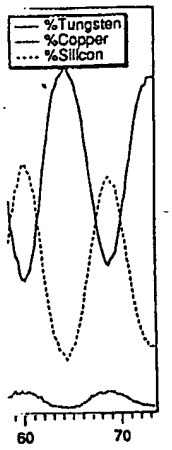

obtained on a

site under these
mple is readily
puttering depth.
n length scale;
ations. Primary
es as a result of
ately 10–20 Å.
ably caused by
onfirm this, the
the sample and

the assumption
is smooth. We
cture of many of
s have a vertical
have found that
being deposited.

lly been the most
crystallographic

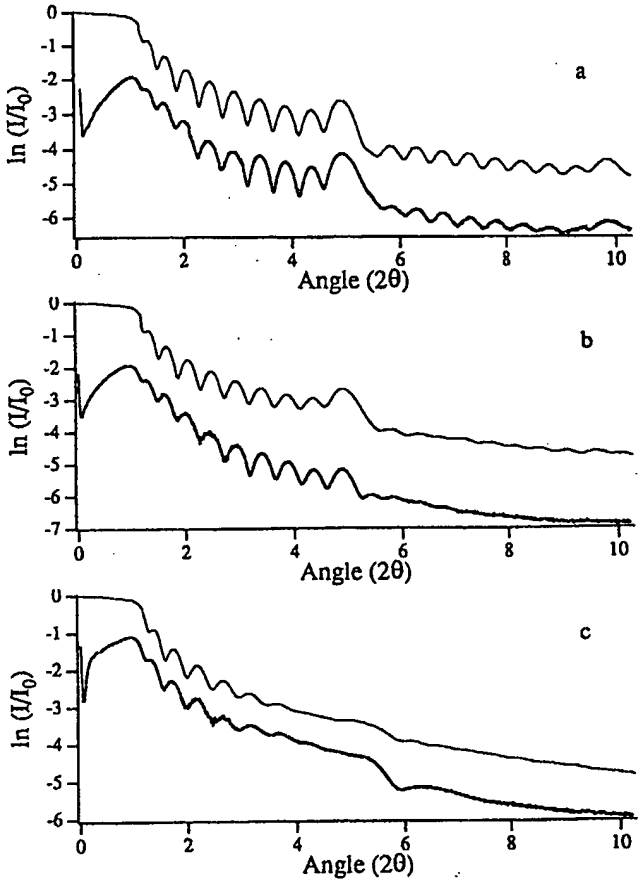

Sputtering Gas	Repeat Thickness	Interdiffusion	Interfacial Roughness from XRD	from TEM
Ar	18	3.0	±2	<3
Kr	18	3.5	±3	3
Xe	16.5	4.0	±6	~10

Figure 21. Experimental diffraction patterns along with the simulated patterns for argon (a), krypton (b), and xenon (c) sputtered multilayer films containing ten bilayers of 4 Å of Co and 13 Å of Pt. The interfacial roughness determined from the simulated patterns agrees well with that determined from the high-resolution transmission electron microscopy studies as summarized in the associated table.

characteristics of multilayers. The major advantage of high-resolution transmission electron microscopy is the ability to view the multilayer in real space with 5 Å resolution. The contrast in bright field imaging is dominated by the crystal lattices of the individual layers and has been used to examine each layer of a multilayer individually and determine the local crystal structure and orientation, layer thickness, and layer roughness [85]. High-angle annular dark-field imaging can be used to determine composition profiles at the interfaces [86]. The major disadvantages of these techniques are the extensive sample preparation required and the small sample area probed with the technique. The extensive sample preparation raises the question of whether the observed structures are inherent in the as-deposited multilayers or result from the mechanical polishing, dimpling, and argon ion milling of the sample to make it electron transparent.

We have used high-resolution transmission electron microscopy as a check of our ability to model low angle diffraction patterns. Our most extensive study was conducted on a series of sputter deposited Pt/Co multilayers prepared by Dr. Carcia [85]. In Carcia's investigation, Ar, Kr, and Xe were used as sputtering gases for the deposition of Pt/Co multilayers containing 10 bilayers of 4 Å of cobalt and 13 Å of platinum. Their high-resolution transmission electron microscopy studies revealed different surface roughnesses depending on the sputtering gas. From the obtained micrographs, the argon-sputtered film had an interfacial roughness of 3 Å over a lateral distance of 100 Å while the xenon-sputtered film had an interfacial roughness of 10 Å over the same lateral distance. Carcia speculated that this roughness was related to the surface diffusion rates of the deposited metals caused by reflected sputter gas atoms bombarding the growing film. The energy of the reflected neutrals decreases with increasing mass of the sputtering atom. The higher surface mobility in argon-sputtered films was thought to result in "layer-like growth" while the lower surface mobilities in the xenon-sputtered films was thought to lead to "island-like growth" [85]. Our modeling of the low-angle diffraction patterns obtained from these films, shown in Figure 21, agrees with the results of the high-resolution transmission electron microscopy study of Carcia.

6. PROBES OF MULTILAYER REACTIONS

Superlattices present several unique opportunities to study solid state reactions. This section describes the use of the analytical tools discussed in Sections 4 and 5 to determine how the structure of buried interfaces changes as the elements interdiffuse and react. The ability to obtain in-depth structural information concerning the development of concentration gradients and interfacial topology via a nondestructive technique is unique to superlattice composites and is essential for the elucidation of a reaction mechanism describing the evolution of the superlattice reactants into products.

In general, knowledge of both the structural and the thermodynamic changes associated with a chemical reaction is desired. In a solid state system, reactions occur only at the interfaces between the reactants. These constitute a very small

fraction of the reacting system, making both structural and thermodynamic information very difficult to obtain. The main advantage realized by the use of superlattice reactants is the concentration of a large number of interfaces within a small volume of sample. The large density of interfaces permits the heat evolved on reaction to be studied using differential scanning calorimetry while the ordered arrangement of the interfaces permits their structure to be determined using low-angle X-ray diffraction.

We obtain an overview of the reaction occurring during the heating of a superlattice by performing a differential scanning calorimetry experiment in conjunction with X-ray diffraction measurements. Differential scanning calorimetry (DSC) is a fast, convenient method of characterizing the thermal evolution of ultrathin-film multilayer composites. It provides information about *when* (at what temperature) phase transformations and various reaction events occur. High-angle X-ray diffraction (XRD), meanwhile, may be used to determine *what* has occurred at these temperatures. Together, DSC and XRD provide a powerful method of following solid state reactions.

These experiments are complemented by variable temperature low-angle diffraction studies of the transition from the initial layered reactant to the homogeneous, amorphous intermediate. The data obtained permit the interdiffusion reaction to be confirmed and quantified. The combined results of these measurements performed on superlattices of different structures permit details of the general reaction mechanism of a solid state reaction to be uncovered. The experimental techniques necessary to perform these measurements on superlattices are described in more detail in the following sections. These are followed by several examples to highlight the utility of these techniques.

6.1. Differential Scanning Calorimetry

In a differential scanning calorimetry experiment, the temperature of a sample and a reference is increased at a constant rate and the temperature difference between them is monitored. If the sample has an exothermic transition, its temperature will be higher than that of the reference. Conversely, if the sample undergoes an endothermic transition, its temperature will be lower than that of the reference. These temperature differences can be converted into enthalpies. A thermogram thus consists of the enthalpy changes in the sample as a function of temperature.

The key experimental factor in obtaining DSC data on superlattices is eliminating the signal damping resulting from the heat capacity of the substrate. This can be done by depositing superlattices upon a polymer-coated substrate and subsequently dissolving away the polymer, leaving a free-standing superlattice.

Differential scanning calorimetry of multilayers prepared in our laboratory is carried out on from 0.25 to 1.5 mg of sample that has been separated from the silicon substrate. Silicon wafers used in the preparation of DSC samples are first coated with a thin film of polymethylmethacrylate (PMMA). A 3% solution of high molecular weight PMMA in chlorobenzene is applied using a spin coater. Virtually

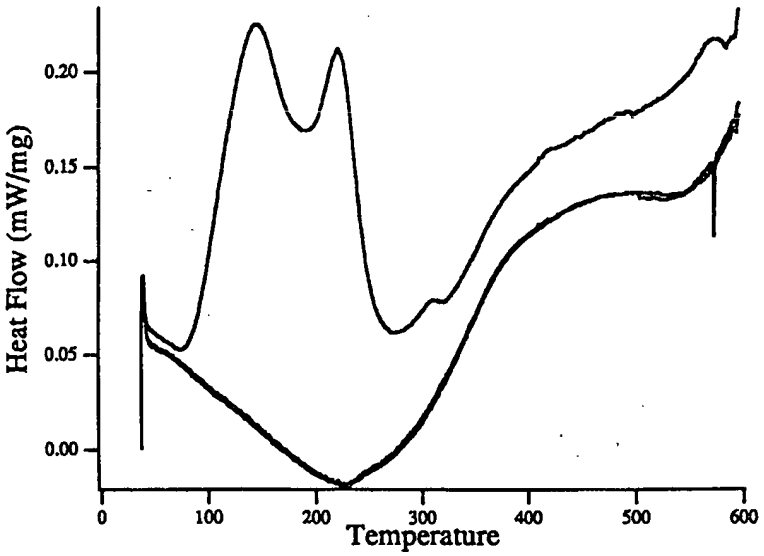

Figure 22. Three sequential thermograms of a molybdenum–selenium superlattice sample. The upper thermogram contains both the reversible and irreversible changes as the sample interdiffuses and crystallizes. Subsequent thermograms are used as a baseline correction for the reversible changes within the reacted sample.

all materials thus far deposited wet the PMMA surface, and no significant degradation of the low-angle diffraction signal arising from the PMMA layer is seen. A multilayer deposited onto a PMMA-coated wafer may be removed from the substrate by soaking in acetone. Depending on the materials used and the stresses inherent in the multilayer, the sample may lift away as one large sheet, which can be transferred into the DSC sample pan with forceps, or as nearly microscopic particles which can be collected only by patient sedimentation, but more typically in a fashion intermediate between these extremes. Once in the pan, the sample is dried under vacuum to remove residual acetone.

The prepared sample pan and an empty reference pan are placed into the DSC cell. Without opening or otherwise disturbing the cell between heating segments, the sample temperature is ramped three times from room temperature to the desired end temperature. This results in three curves, as illustrated in Figure 22 for a molybdenum–selenium sample. The signal caused by heat flow into or out of the sample is superimposed on the curved baseline characteristic of the DSC cell and sample pans. To reject any signal that does not originate from the sample, the third (last run) curve is subtracted from both the first and second curves. This yields the two curves illustrated in Figure 23. The topmost of these curves, which results from

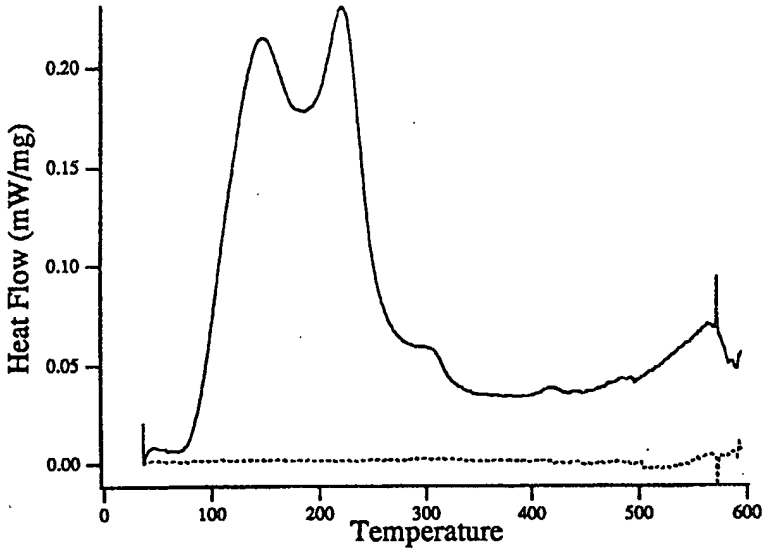

Figure 23. Two curves resulting from the subtraction of the thermograms shown in Figure 22. The upper curve is the subtraction of the third thermogram from the first and contains the irreversible changes in the sample as it is initially heated. The lower curve is obtained from subtracting the third thermogram from the second and is an effective baseline for this sequence of thermograms.

subtracting the last from the first data curve, shows the signal corresponding to irreversible changes in the sample. The fact that the lower of the two derived curves is nearly horizontal shows that the solid state reaction went to completion during the first heating of the sample.

Although this method is a quite satisfactory means of separating the signal originating in the sample from that due to the instrument, several complications should be noted. In virtually every case, the transformation of the as-deposited multilayer into a crystalline solid is accompanied by a change in heat capacity due to the large changes in bonding. This results in the offset observed between the first and subsequent thermograms in Figure 23. Although this in no way affects the qualitative interpretation of the data, it does complicate the quantitative analysis. Because DSC measures heat flow, it is possible to obtain the enthalpy of a transition by integrating the area under a peak. A large change in heat capacity can confuse where one ought to draw the bottom of the peak and can lead to substantial uncertainty in the value found for the enthalpy change. A second complication arises when reversible phase transitions are present. For instance, if the crystalline phase formed in the first heating of the sample melts at a temperature lower than the maximum temperature used in the experiment, endothermic peaks will appear

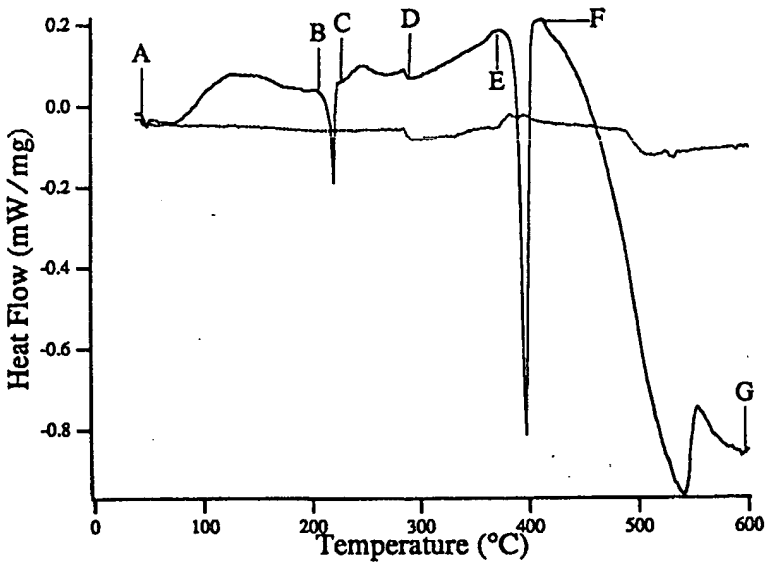

Figure 24. Thermogram of a vanadium/selenium superlattice reactant collected by increasing the temperature 10°C/min and detecting the heat emitted or adsorbed by the sample. At the points labeled A–G, diffraction data were collected and the diffraction patterns obtained are presented in Figure 25.

in the second and third data curves, which may not be present in the first curve. In that case, when the curves are subtracted, a false exotherm will appear in the signal curve, and no peak will appear in the background curve. A third problem is that the sample can react with the DSC pans. This is typically seen when using metal pans and temperatures above 500°C [87].

To illustrate how differential scanning calorimetry and high-angle X-ray diffraction are used in conjunction, a thermogram of a vanadium/selenium superlattice sample is shown in Figure 24. Although this thermogram contains several clearly separate exotherms and endotherms, the DSC data are insufficient to determine the cause of these peaks. X-ray diffraction carried out at the points marked A through G, shown in Figure 25, provides the missing information. The low-angle diffractogram taken at A shows superlattice Bragg peaks, indicating that the sample is layered. The high-angle diffraction pattern, also taken at A, shows no crystalline features, implying that the individual layers in the multilayer are amorphous. The endotherm at 220°C is associated with phase separation of the sample and the subsequent melting of selenium as expected from the vanadium–selenium phase diagram. After the small exotherm from 235°–300°C, the high-angle diffraction

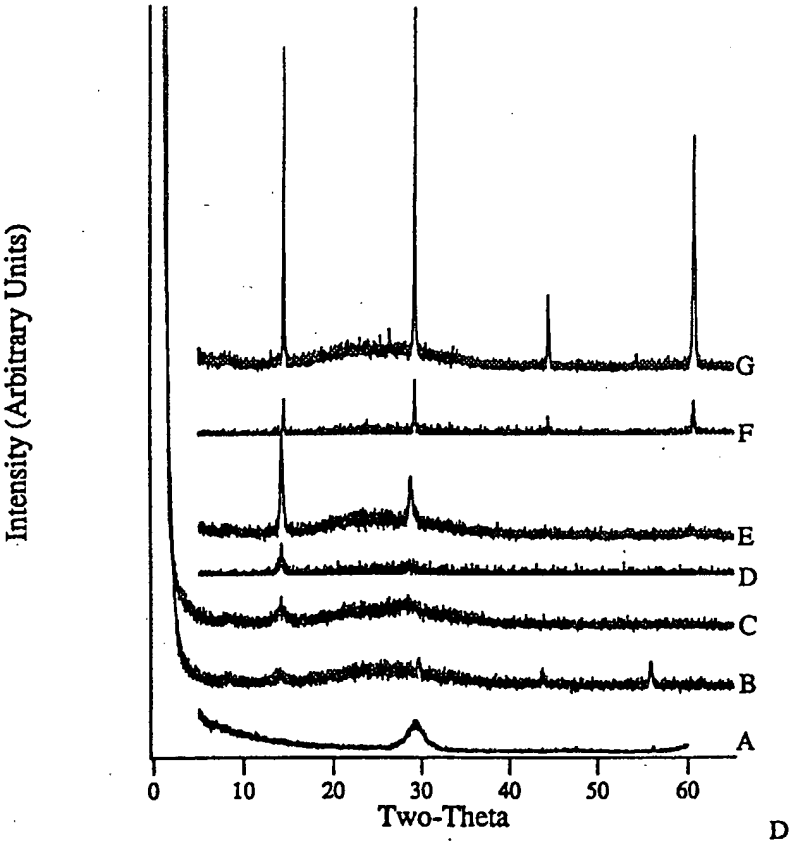

Figure 25. Diffraction data collected on a vanadium/selenium superlattice reactant at the points labeled A–G in the thermogram shown in Figure 24.

pattern shows peaks characteristic of the compound V_2Se_9. Thus, the first, lower temperature exotherm corresponds to diffusion while the second corresponds to nucleation and growth of V_2Se_9. The endotherm at 400°C is due to the decomposition of V_2Se_9 and the vaporization of selenium, as expected from the phase diagram. The vaporization of selenium was confirmed by mass loss observed in thermal gravimetric analysis coincident with the deposition of amorphous red selenium. The diffraction pattern of the sample after this endotherm is consistent with that expected for vanadium diselenide.

6.2. Variable Temperature Diffracti n

The differential scanning calorimetry experiments are extremely useful in determining the gross changes in superlattice reactants on heating, but they do not provide any structural information concerning how the transformation from a superlattice to a uniformly mixed amorphous intermediate or crystalline compound occurs. Studies directed at observing the initial evolution of solid–solid interfaces have been limited to length scales above 20 Å due to the lack of a suitable probe. Sputter depth profiling Auger electron spectroscopy [88] and Rutherford backscattering [89,90] have been useful in monitoring interfaces on longer length scales, but they yield little information regarding the initial reaction of two solid reactants.

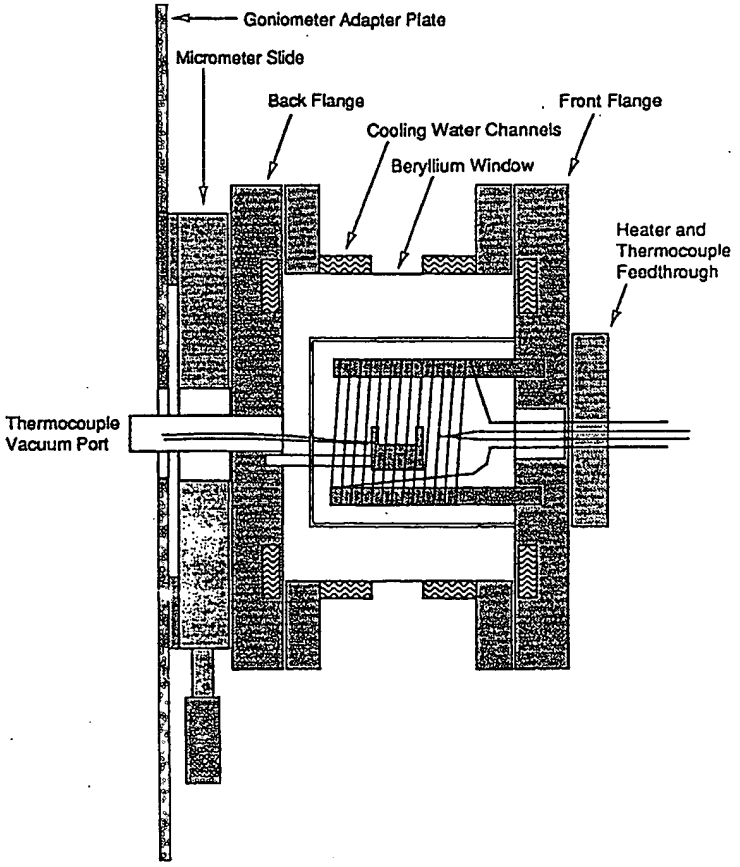

Figure 26. Schematic of the assembled high-temperature diffraction camera used in our studies.

The decay of superlattice reflections as a result of interdiffusion is the most sensitive method available to monitor interfacial structure at reacting interfaces [91]. The ability to perform this experiment is a major advantage to using superlattices as initial reactants for the formation of amorphous intermediates.

The basis for this experiment is simple. The diffraction pattern from the initial multilayer must disappear as interdiffusion of the elemental layers occurs. Variable temperature low-angle diffraction experiments are very sensitive to the structure and composition of the interface regions within a superlattice composite. The difficulties associated with variable temperature, low-angle diffraction experiments result from the need to quantify the intensity of the superlattice reflections. These intensities are exceedingly sensitive to alignment as demonstrated earlier; maintaining alignment becomes much more difficult when varying the temperature.

We designed a high-temperature, controlled atmosphere chamber which attaches to the backplate of the room-temperature sample mounting assembly. This system permits the rapid alignment of the high-temperature assembly, shown in Figure 26, and minimizes difficulties associated with the transition between room-temperature and high-temperature data collection. Data are obtained with this system by monitoring the change in diffraction intensities as a function of time while maintaining a constant temperature. Figure 27 contains an example of the changes in the intensity of low-angle diffraction signals in an iron–silicon superlattice on low-temperature annealing.

Analysis of Diffusion Data

The analysis of the decay of diffraction intensity with time and temperature was originally discussed by Dumond and Youtz, who prepared multilayers for use as X-ray mirrors only to find that the reflectivity of the mirrors decayed as a function of time due to interdiffusion [92]. In this initial investigation, and the majority of those that followed, only the intensity of the first-order Bragg reflections were followed as a function of temperature and time, yielding only the interdiffusion rates. Following the lead of Fleming et al. [93], we have followed the decay of all the observable diffraction orders with time, permitting the evolution of interfacial structure with annealing to be studied.

The mathematical formulation of the manner in which concentration differences disappear as a result of diffusion is known as Fick's first and second laws of diffusion. Fick's laws of diffusion are a phenomenological model originally developed for high-temperature diffusion over relatively long distances [91]. The one-dimensional form of Fick's second law is

$$\frac{\partial}{\partial t} c(x,t) = \frac{\partial}{\partial x}\left[\frac{\partial}{\partial x} k(x)c(x,t)\right], \tag{9}$$

where $c(x,t)$ is the concentration, $k(x)$ is the interdiffusion coefficient, x is a spatial coordinate normal to the surface of the composite, and t is time. The derivation of

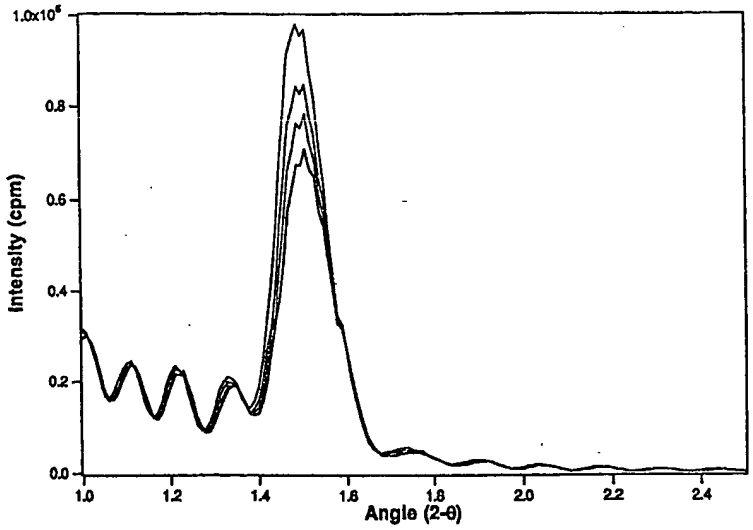

Figure 27. Series of grazing-angle X-ray diffraction scans of an Fe–Si composite taken as a function of temperature and time, illustrating the decay of the diffraction signal intensity without broadening. The peak at 1.5° is the first-order Bragg peak. The smaller peaks arise from the finite number of layers in the sample, and their constant intensity implies that the sample maintains coherency during the diffusion process.

this equation assumes that there is a chemical potential gradient across the region of varying composition, that the diffusion medium is a continuum, and that higher order terms in the concentration gradient can be neglected.

The simplest approach to quantitatively describe diffusion is to assume a concentration-independent interdiffusion coefficient for a particular interface which depends only on temperature. The interdiffusion coefficient is the sum of the diffusion of the various elements in the diffusion couple and the migration of vacancies. This approximation is most appropriate when the diffusion constant of A into B and B into A are of the same magnitude. If one also assumes that the interdiffusion coefficient is independent of position (and therefore independent of composition), Equation (9) simplifies to

$$\frac{\partial}{\partial t} = D\frac{\partial^2 c}{\partial_x{}^2}. \tag{10}$$

By using the relationship between diffraction intensity and Fourier expansion coefficients of the concentration profile [Equations (5) and (7)], it is easily shown that the intensity of the superlattice Bragg diffraction peaks should decay according to

$$\frac{d}{dt}\left[\ln\left(\frac{I}{I_0}\right)\right]=\frac{-8\pi^2n^2}{d^2}D, \tag{11}$$

where d is the length of the repeat unit in the superlattice and n is the order of each of the Bragg reflections [94]. Each Bragg reflection should decay at a rate such that each decay produces the same diffusion coefficient. Equation (11) predicts that the second-order Bragg diffraction peak should decay four times faster than the first-order reflection. A plot of $\ln[(I)/I_0]$ versus $(-8\pi^2n^2/d^2)\gamma$ should yield the same straight line for all Bragg reflections, the slope of which is the interdiffusion coefficient, D.

This result permits interdiffusion coefficients to be determined, but the strict applicability of this solution is limited due to the approximations made in its derivation. In particular, the assumption of a concentration-independent interdiffusion coefficient does not reflect the more complicated interdiffusion process found in most diffusion couples, resulting in deviations from Equation (11).

Examples

We have collected extensive interdiffusion data from the reaction of several binary superlattices at low temperatures [95–97]. The following analysis of two of these data sets highlights the ability to obtain quantitative information concerning the evolution of a solid state reaction from variable temperature diffraction experiments. This information is impossible or exceedingly difficult to obtain via other techniques.

Iron–Silicon Interdiffusion

The simplest system from an interdiffusion standpoint that we have investigated to date is that of iron and silicon. From a differential scanning calorimetry experiment, interdiffusion of iron and silicon was expected to begin at approximately 100°C. In our initial investigation of this system, the decay of the superlattice Bragg reflections with time due to interdiffusion of iron and silicon at 150°C was observed, as shown in Figure 27.

Several qualitative conclusions can be drawn from the iron–silicon interdiffusion data. Most important, these data indicate that the interdiffusion process is coherent, that is, that the electron density profiles at each interface change at the same rate as a function of temperature and time. The peak width at half maximum of the Bragg diffraction maxima does not change as the signal decays with time, indicating that there is no broadening in the distribution of unit cells with respect to unit cell size or electron density distribution. Also, the intensity of the subsidiary maxima does not change with time, even while the intensity of the Bragg diffraction maxima decrease due to interdiffusion. Equation (5) implies that if all else is equal, the subsidiary maxima should also decrease in proportion to the Bragg maxima. The constant intensity of the subsidiary maxima suggests that the interdiffusion at the interfaces has reduced the incoherent roughness.

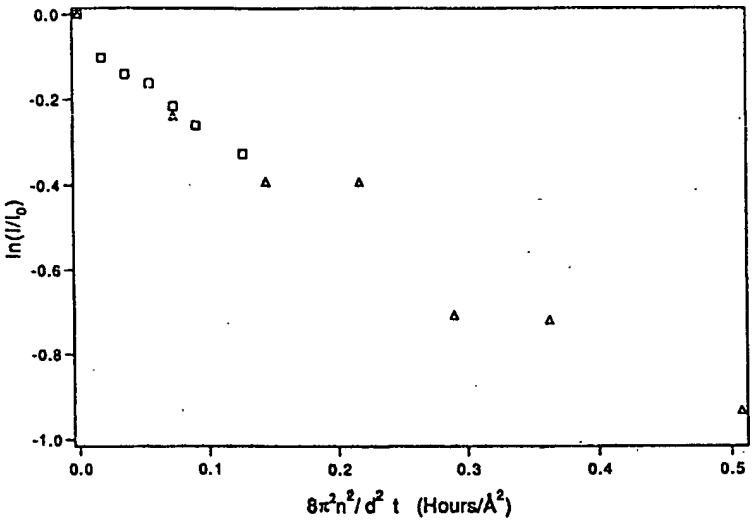

Figure 28. Variation of the intensities of the first- (□) and second-order (△) Bragg peaks in an iron–silicon modulated film annealed at 150°C. Slope of $\ln(I/I_0)$ vs. β_1^2 plot, where $\beta = 2\pi/d$, yields an interdiffusion coefficient of 1.3×10^{-19} cm^2/sec.

The intensity data given in Figure 27 for the iron–silicon composite are replotted according to Equation (10) in Figure 28. The diffraction data for the two diffraction orders studied fall on the same line, indicating that the simple picture described above is adequate in explaining our initial experimental results. As expected, the second-order diffraction peak decays four times faster than the first-order diffraction peak. The slope of these lines gives the interdiffusion coefficient for this diffusion couple as 1.3×10^{-19} cm^2/sec at 150°C. In an attempt to determine an activation energy for the interdiffusion process, a subsequent, more complete data set on the same iron–silicon composite was collected.

Interdiffusion was monitored at 100°, 110°, 135°, and 159°C for 12 hr (see Fig. 29). These data contain several discrepancies from the simple interdiffusion suggested by the initial data collected at 150°C. For the three highest temperatures, the second-order Bragg reflection initially decays four times faster than the first-order Bragg reflection, as expected from the initial experiment at 150°C. At 100°C, however, the second-order Bragg reflection decays more slowly than expected, indicating a possible composition dependence on the interdiffusion process.

The data also deviate from Equation (3) at long times for each of the data sets. The diffusion process appears to slow down as the sample is annealed at a particular temperature. Previous diffraction studies on the decay of metal–metal superlattice

Δ) Bragg peaks
β_t^2 plot, where

are replotted
wo diffraction
ure described
expected, the
order diffrac-
icient for this
determine an
complete data

12 hr (see Fig.
interdiffusion
temperatures,
ster than the
at 150°C. At
slowly than
interdiffusion

the data sets.
at a particular
al superlattice

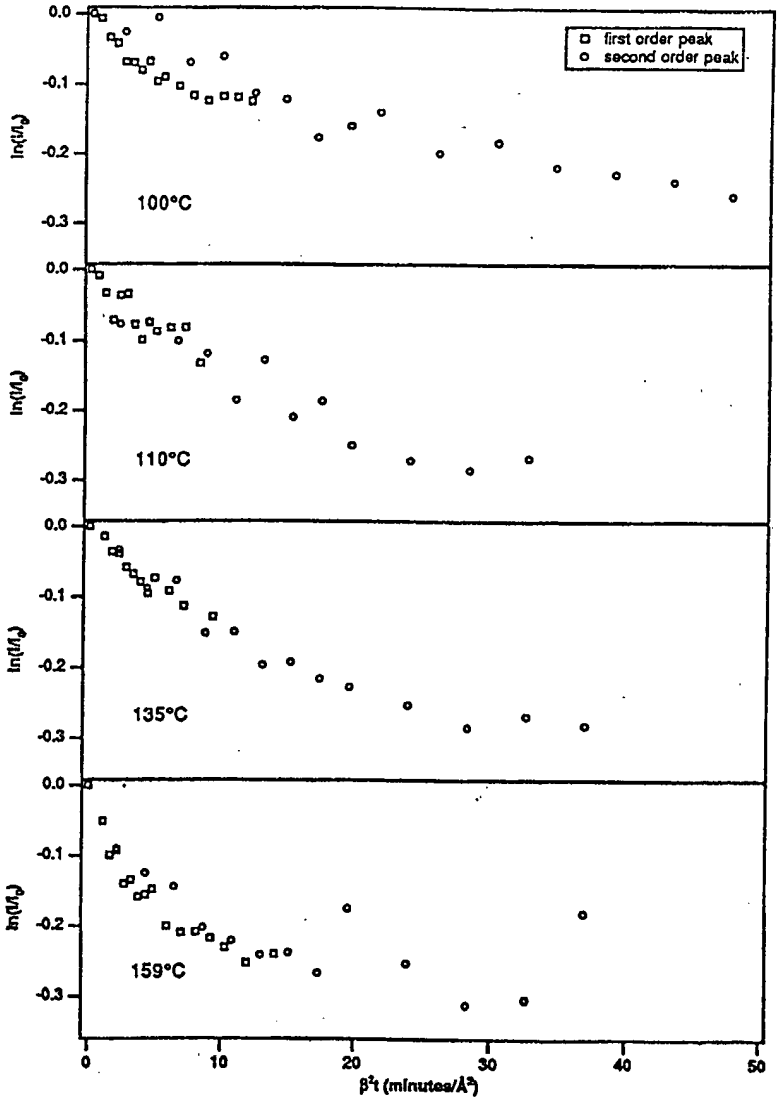

Figure 29. Variation of the intensities of the first- (○) and second-order (□) Bragg peaks in a iron–silicon modulated film with time when annealed at the indicated temperatures. Data are plotted as $\ln(I/I_0)$ vs. β_t^2 to emphasize the deviations from Fick's second law of diffusion.

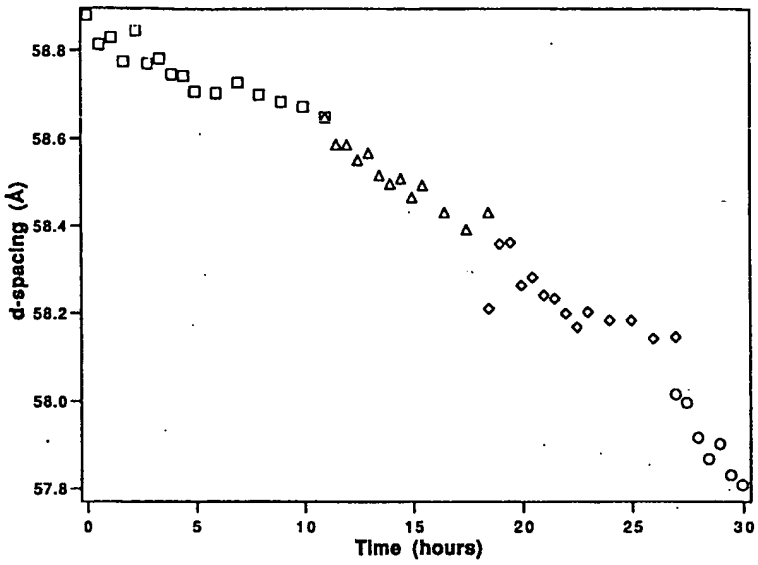

Figure 30. Variation in the position of the first-order Bragg reflection of an iron–silicon modulated film as a function of annealing at 100°C (□), 110°C (△), 135°C (◇), and 159°C (○). The shift in the position of this reflection is proportional to the decrease in the size of the repeat unit during the interdiffusion of the superlattice.

reflections as a function of time have also shown an initial fast diffusion process followed by a slower, limiting diffusion rate [98]. It was suggested that the change in the diffusion rate with time might be due to either changes in microstructure or changes in the macroscopic stresses in the superlattice. We believe that the decrease in the diffusion rate is caused by elimination of defects and a corresponding increase in the activation energy for diffusion due to the selective elimination of the most mobile and energetically unfavored conformations. The amorphous modulated composites are internally unstable in that they continuously transform to amorphous states of lower free energy.

The decrease in the number of high-energy conformations and voids with time and temperature is given strong support by the decrease in the unit cell size with time, as shown in Figure 30. The initially deposited composites have a very nonequilibrium distribution of conformations. A high concentration of voids and other unstable conformations is present in the composite as a result of the quenching of the atoms from the gas phase onto the deposition surface. Diffusion occurs through energetically accessible defects. As the temperature is raised, new conformations become accessible as diffusion pathways. The concentration of these conformations decrease with time as the most energetically unfavorable pathways

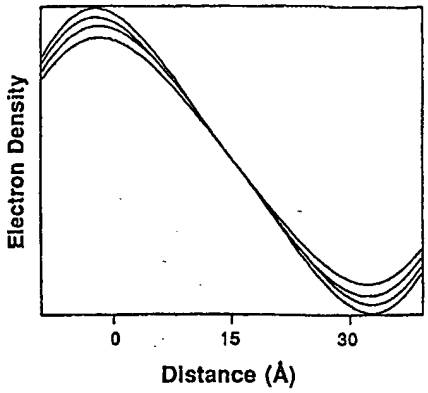

Figure 31. Schematic of the evolution of an Fe–Si interface using intensity data and an arbitrary phase relationship.

are eliminated. Since the number of diffusion paths as well as the energy available are changing with time and temperature in these experiments, an activation energy for the interdiffusion process cannot be determined from an Arrhenius expression.

The data described above suggest the following picture for the evolution of the composite. As the temperature is raised, the composite lowers its total energy through the elimination of high energy conformations frozen in the composite during deposition and by the lowering of chemical potential due to the mixing of the elements. This diffusion-limited process continues until the initial structural modulation has been completely diffused away.

An electron density profile of the evolution of the interface region can be created by assigning phase information to the intensity data. Figure 31 contains the changes in the electron density with distance on annealing for the iron–silicon system, assuming that the structures are centrosymmetric and using the phase relationship given by an atomically abrupt interface. The interdiffusion process is a simple and gradual decay in the electron density gradient with time. This simple picture of iron–silicon interdiffusion was found to occur across this phase diagram as long as the total thickness of the bilayers was less than 80 Å. This mixing can account for up to 90% of the total heat of formation of crystalline iron silicide [96].

Titanium–Silicon Interdiffusion

To expand upon these observations, we investigated a more reactive silicide system. The titanium–silicon system was chosen since titanium and silicon react approximately four times more exothermically than iron and silicon [99]. This increased reactivity offered an opportunity to study a system in which chemical bonding differences with composition should play a larger role in the interdiffusion reaction.

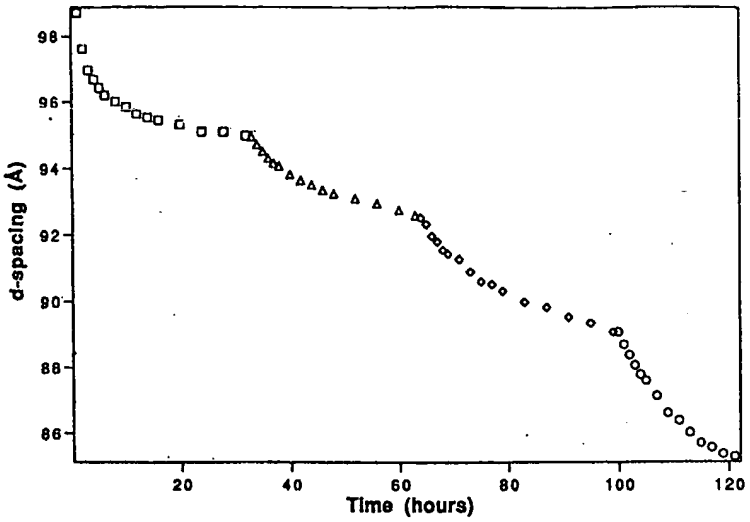

Figure 32. Variation in the thickness of the multilayer spacing as calculated from the position of the first-order Bragg reflection of a titanium–silicon sample. Data were collected while annealing sample at 217°C (□), 244°C (△), 271°C (◇), and 298°C (○).

The titanium–silicon system diffraction data again suggest that diffusion is coherent, since the line widths of the Bragg diffraction peaks do not change with time. As with the iron–silicon sample, the size of the unit cell was found to decrease during annealing. A change of nearly 16% was observed over the course of the experiment (Fig. 32), in agreement with previous studies [100]. The size decrease results from the increased density of the binary alloy relative to unreacted titanium and silicon layers in addition to the elimination of low-density configurations.

To confirm that diffusion paths are indeed being eliminated during the annealing process, an as-deposited titanium–silicon sample and one preannealed at 244°C were annealed at 271°C. Intensities of the first-order Bragg peak as a function of time are shown in Figure 33. The initial diffusion rate is a factor of five higher in the sample heated immediately to 271°C, but the data at longer times are virtually identical for both samples. This suggests that annealing of the composites selectively eliminates low activation energy diffusion paths.

Evidence for dramatic changes in the structure of the composite during interdiffusion is found in the changes in the Bragg intensities with time at various temperatures, as plotted in Figure 34. The intensities of the second-order Bragg reflections actually increase during low-temperature annealing. The growth of this Bragg reflection results from developing structure or asymmetry of the evolving interface. This implies that the interdiffusion coefficient is not independent of composition [93].

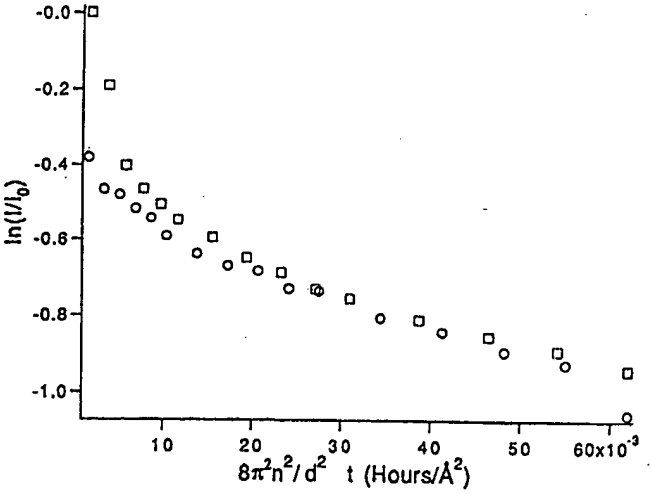

Figure 33. Variation of the intensity of the first-order Bragg peak in a titanium–silicon modulated film as-deposited and annealed at 271°C (□), and preannealed at 244°C then annealed at 271°C (○).

The compositional dependence on the diffusion constant is chemically reasonable given the large variation in formation enthalpies in titanium silicides [101]. Amorphous alloys of different composition will also have different formation energies. At low temperatures, the free energy is dominated by ΔH, so large differences in ΔH relative to $T\Delta S$ can lead to the growth of a plateau in composition. This interpretation is supported by the changes in the electron density with distance on annealing, pictured in Figure 35, which clearly shows the formation of a compositional plateau at the interface.

Summary

The artificial structure of superlattice reactants is ideally suited for detailed investigations into the mechanism of their reaction. Calorimetery permits the heat evolved as a function of temperature to be quantified. Combined with X-ray diffraction it permits the sequence of reaction events and structure of reaction intermediates to be identified. Variable-temperature low-angle X-ray diffraction permits the initial stages of a solid state reaction to be explored. This technique is exquisitely sensitive to interdiffusion of the initial layered elements. By measuring diffraction intensities as a function of time and temperature, the composition gradients at the reacting interfaces can be followed as intermediate structures evolve during interdiffusion. The ability to follow these interdiffusion reactions on a 10 Å length scale is unique and makes superlattice reactants an ideal initial reactant for the study of solid state reaction mechanisms.

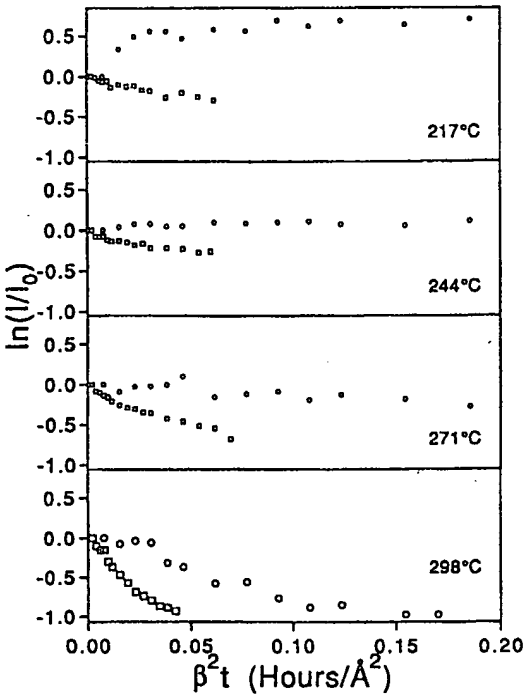

Figure 34. Variation of the intensities of the first- (o) and second-order (□) Bragg peaks in a titanium–silicon modulated film with time when annealed at the indicated temperatures. Data are plotted as $\ln(I/I_0)$ vs. $\beta^2 t$ to emphasize the deviations from Fick's second law of diffusion.

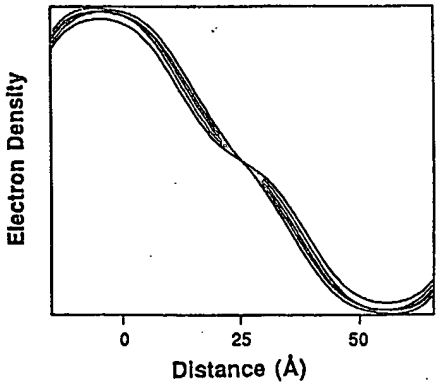

Figure 35. Schematic of the evolution of a Ti–Si interface using intensity data and an arbitrary phase relationship.

7. CONTROLLING SOLID STATE REACTIONS VIA RATIONAL DESIGN OF SUPERLATTICE REACTANTS

The ultimate goal of the work described in this chapter is to develop a synthetic strategy to prepare metastable compounds under reaction conditions where they are unstable. The proposed route contains several key steps, all based on the assumption that one can control a solid state reaction mechanism via the structure of the initial superlattice reactant. The first step in the proposed mechanism is the interdiffusion of a superlattice into a homogeneous, amorphous reaction intermediate. The preparation of such an amorphous intermediate via structural design of the initial superlattice reactant is discussed in Section 7.1. The second step involves control of the crystallization of the amorphous reaction intermediate so that the desired compound is obtained. In binary systems, this entails the ability to crystallize a particular binary compound from the amorphous intermediate without the formation of any other crystalline compound. The ability to control the nucleation of the amorphous intermediate via composition is the subject of Section 7.2. In Section 7.3, the importance of both these steps is reinforced by a series of experiments conducted on the binary iron/aluminum system. The initial reaction step in this system, the nucleation of FeAl, has not been controlled via composition or bilayer thickness. This result is used to highlight the importance of the extra degree of freedom in ternary superlattices, the deposition order, in designing a superlattice reactant which will evolve to an amorphous intermediate.

In a ternary system, the challenge is to crystallize the desired ternary compound without the formation of crystalline, binary compounds as reaction intermediates. The synthesis of a particular ternary compound, $Cu_2Mo_6Se_8$, without the formation of crystalline binary intermediates, is discussed in Section 7.4.

7.1. Effect of Length Scale on the Mechanism of a Solid State Reaction

The initial stage of a solid state reaction is the formation of an amorphous alloy at the interface between two reacting elements, lowering the free energy of the system. This involves a competition between diffusion and nucleation. The relative activation energies of both these processes depend on the structure of the interface as well as the rest of the composite. The activation energy for diffusion within a superlattice increases with annealing as high-energy configurations are eliminated. The activation energy for nucleation is affected by the structure of the interface and the stresses and strains present at the interface. As the interfacial stresses and strains and the interfaces themselves are eliminated by diffusion, the activation energy for nucleation will increase. The changing energetics of both diffusion and nucleation suggest that a critical superlattice repeat distance could exist below which the resulting films should evolve into a metastable amorphous state. This critical distance will be very dependent on the crystal chemistry of the compounds in the phase diagram of interest.

In systems with large structural differences between the amorphous alloy and the crystalline compound, there will be an appreciable driving force for the crystallization of the amorphous alloy formed in the interfacial region. If the resulting structure is a simple one, this will result in a small critical distance. The driving force can be thought of as resulting from the directional nature of covalent bonding, with large energy differences associated with relatively small angular or bond distance changes from optimal values. This directional bonding will result in a smaller angular and bond distance distribution than would be found in a metal–metal alloy system with mainly metallic bonding.

Molybdenum Diselenide

$MoSe_2$ is an example of a compound with highly directional bonding. Its structure is far from that found in metal–metal alloys, consisting of a hexagonal plane of molybdenum atoms capped on either side by hexagonal nets of selenium. These sandwich-like layers then stack to form the $MoSe_2$ structure. A previous investigation [102] and our own studies indicated that $MoSe_2$ crystallizes at very low temperatures (~200°C) in thin-film diffusion couples. The low nucleation

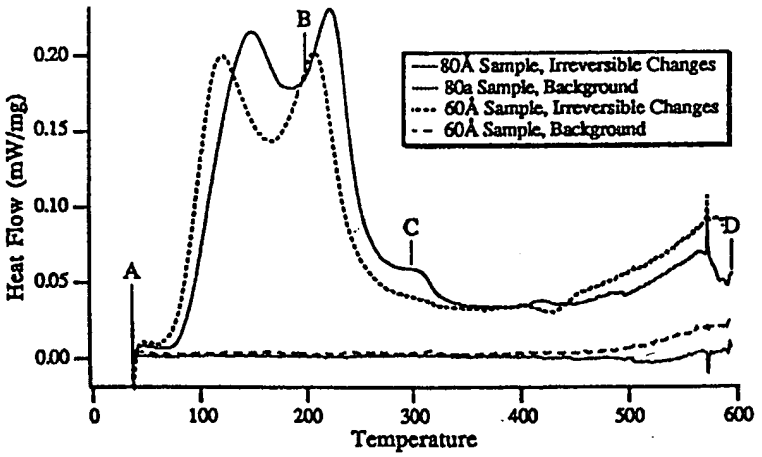

Figure 36. Thermograms obtained for the molybdenum selenium superlattices with repeat distances of 60 and 80 Å. The upper curves are obtained by subtracting the third thermogram from the first and contain the irreversible changes in the samples as they are initially heated. The lower curves are obtained by subtracting the second thermogram from the third and are an effective baseline for this sequence of thermograms. At the points labeled A–D, diffraction data were collected and the diffraction patterns obtained are presented in Figure 37.

temperature for molybdenum diselenide is a consequence of the small crystallographic unit cell, its two-dimensional structure, and its large heat of formation from the elements. In addition, molybdenum selenium compounds decompose at temperatures above 1400°C, forming solid molybdenum and selenium vapor. Since all these properties are inherent to the system, formation of an amorphous, molybdenum–selenium alloy by melt spinning or codeposition is predicted to be impossible. Preparation of an amorphous alloy in this system via a solid state interdiffusion reaction represents a significant synthetic challenge.

A series of molybdenum–selenium samples of identical composition, but varying modulation length, were prepared via high vacuum deposition to probe the effect of layer thickness on the solid state reaction [103]. Differential scanning calorimetry and high-angle X-ray diffraction were used to investigate the reaction pathway of the multilayer composites. Two limiting behaviors were observed. Superlattices of molybdenum and selenium with a layer spacing larger than 38 Å behaved as thin-film diffusion couples. Figure 36 shows the heat evolution as a function of temperature for the composites with layer spacings of 60 and 80 Å. Each of these data sets contains two overlapping exotherms below 250°C. Diffraction data collected on samples heated to the points A, B, C, and D indicated in Figure 36 are shown in Figure 37. These data, combined with low-angle diffraction studies, demonstrate that the first exotherm is due to diffusion and the second exotherm results from the nucleation and growth of $MoSe_2$.

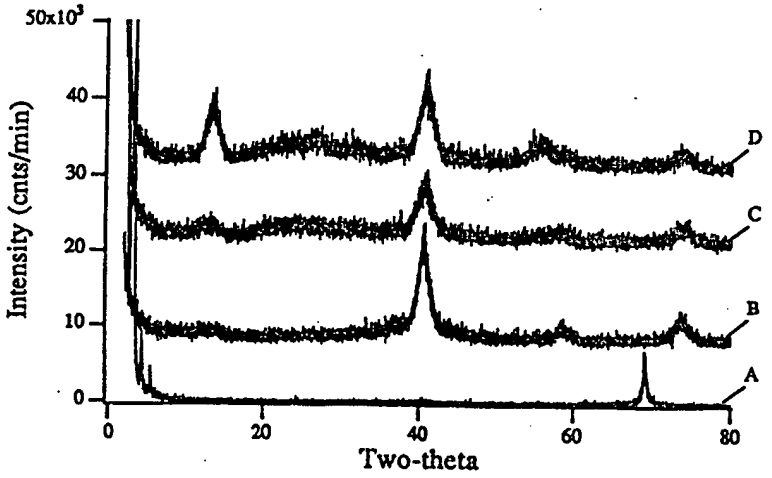

Figure 37. Diffraction data obtained on the molybdenum–selenium superlattice with a repeating distance of 80 Å at the temperatures indicated on Figure 36. The diffraction lines present at high angles are the 00l lines of $MoSe_2$. The absence of other diffraction lines suggest that the compound has grown with a preferred orientation. The peak at 72° on diffraction pattern A is due to the silicon wafer. The curves are offset vertically for clarity.

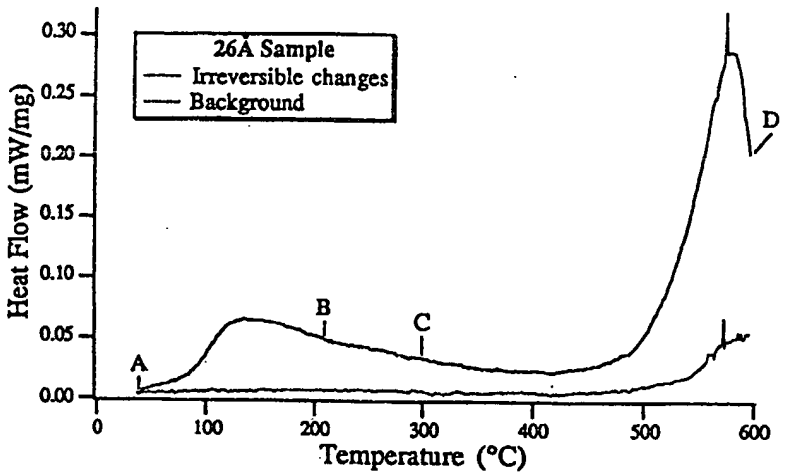

Figure 38. Thermograms obtained for the molybdenum–selenium superlattice with a repeat distance of 26 Å. The upper curve is obtained by subtracting the third thermogram from the first and contains the irreversible changes in the sample as it is initially heated. The lower curve is obtained by subtracting the second thermogram from the third and is an effective baseline for this sequence of thermograms. At the points labeled A–D, diffraction data were collected and the diffraction patterns obtained are presented in Figure 39.

The behavior observed for composites of 27 Å or less in modulation length is distinctly different, as illustrated by the differential scanning calorimetry data for a 26 Å repeat unit shown in Figure 38. These data are characteristic of samples in this length regime and contain a broad maximum beginning at 100°C followed by a large exotherm with a maximum at 575°C. Figure 39 shows diffraction data collected on samples heated to points A, B, C, and D in Figure 38. The first broad exotherm results from the interdiffusion of the molybdenum and selenium layers. Annealing the sample for 26 hr at 350°C eliminates the low-angle superlattice reflections without the crystallization of $MoSe_2$. Crystalline $MoSe_2$ is observed only after the large exotherm at 575°C.

There is a surprisingly large difference in the nucleation temperatures for composites in these two different length scale regimes. This large difference can be understood by considering the factors affecting nucleation within a solid matrix [104]. The conversion of the metastable amorphous intermediate into a thermodynamically more stable crystalline product initially begins on a very small scale due to entropy considerations. This nucleation step involves the assemblage of the proper kinds of atoms via diffusion, structural rearrangement into intermediates, and the formation of stable nuclei [28].

In the composites with bilayer thickness above 38 Å, nucleation occurs in the concentration gradient at the interface. The composition gradients enhance diffu-

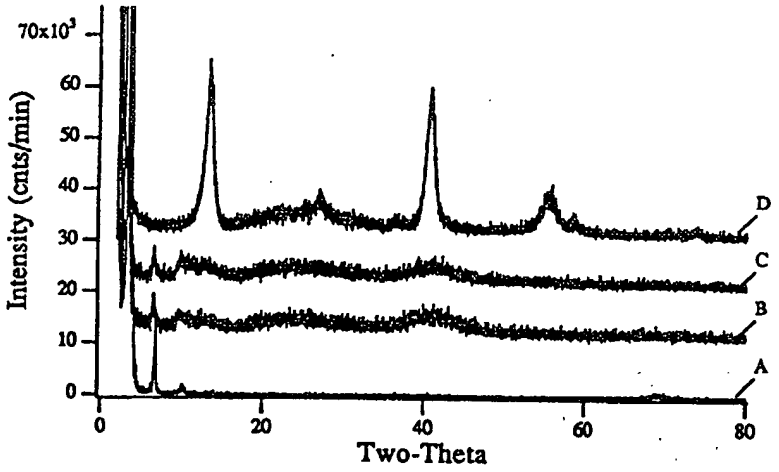

Figure 39. Diffraction data obtained on the molybdenum–selenium superlattice with a repeating distance of 26 Å at the temperatures indicated on Figure 38. The diffraction lines present at high angles in the scan taken at 600°C are the 00l lines of $MoSe_2$. The absence of other diffraction lines suggest that the compound has grown with a preferred orientation. The curves are offset vertically for clarity.

sion rates, while the interdiffusion of the elements can result in local stresses and strains. These effects combine to lower the surface energy component for nucleation at interfaces, making nucleation easier in this region. This agrees with the observation that crystalline compounds preferentially nucleate at interfaces and surfaces [8,44,105] and with our own observations that nucleation occurs at lower temperatures in the longer length scale regime.

Low-angle diffraction data collected on the 80 Å sample as a function of temperature from 100° to 184°C support this picture. The first-order peak is seen to decrease as expected but the second-order diffraction peak grows with time, as seen in Figure 40. This indicates that a plateau of composition develops in the interface region as the amorphous interface expands [93,95,97]. Once this plateau reaches a critical size, $MoSe_2$ is observed to nucleate and grow, resulting in the second exotherm. Thus, a layered Mo–Se composite with a repeat unit of approximately 38 Å or greater behaves as if each interface were a thin-film diffusion couple.

In the ultrathin-film regime, nucleation occurs after diffusion is complete. Low-angle diffraction data collected as a function of temperature from 109° to 222°C confirm that the first exotherm is due to the initial interdiffusion of the layers. The intensities of the low-angle diffraction peaks are plotted in Figure 41. Compared with the 80 Å composite discussed earlier, the plateau growth is severely

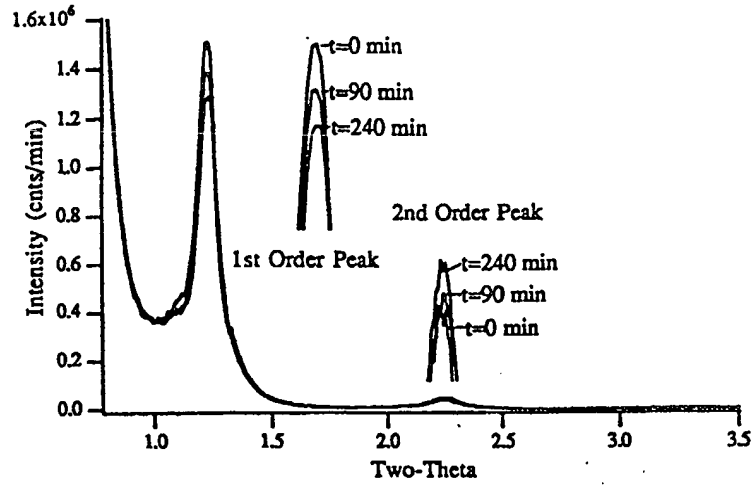

Figure 40. Low-angle diffraction data collected on a molybdenum–selenium superlattice with a repeating distance of 80 Å while being annealed at 184°C. The data were collected at $t = 0$, 90, and 240 min.

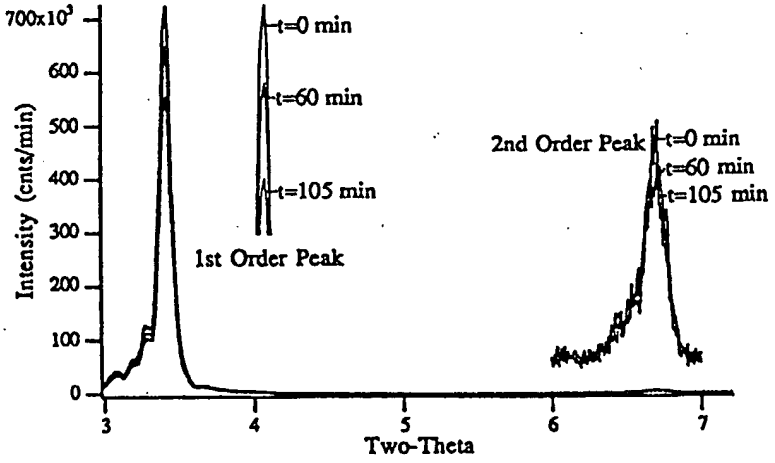

Figure 41. Low-angle diffraction data collected on a molybdenum–selenium superlattice with a repeating distance of 26 Å while being annealed at 222°C. The data were collected at $t = 0$, 60, and 105 min.

depressed, as indicated by the decay of the second-order diffraction peak with time. High-angle diffraction scans indicate that the sample remains amorphous as the sample completely interdiffuses. Since all the interfaces have diffused away, nucleation of a binary phase is more difficult due to the disappearance of long-range stresses and strains inherent in the interface regions. This is more like the case of homogenous nucleation, discussed in the background section of this chapter and shown in Figure 5.

These results demonstrate that the course of a solid state reaction can be controlled by varying the length scale of the initial composite. The ability to follow the reaction of a superlattice via DSC and low-angle X-ray diffraction is essential to understanding the differences in the mechanisms of the solid state interdiffusion reactions and how the mechanisms change with initial superlattice structure. To summarize, the first key synthetic step in the proposed mechanism (Figure 6), the formation of an amorphous intermediate, can be accomplished by the design of the starting superlattice. For binary superlattices, the only adjustable parameter is the thickness of the respective elemental layers. The next step, controlling the nucleation of the amorphous intermediate to obtain the desired compound, is the subject of the next section.

7.2. Composition-Controlled Crystallization of Binary, Amorphous Reaction Intermediates

The results presented in Section 7.1 appear to be general, in that most combinations of elements can be made into an amorphous alloy by the design of an appropriate structure for the initial multilayer. This section addresses the ability to control the crystallization of the amorphous reaction intermediate so that the desired compound is obtained. Data are presented indicating that nucleation of the amorphous intermediates prepared from superlattices layered below the critical distance can be controlled by their composition [96].

The strategy used in these studies is to prepare superlattices of varying composition by changing the relative layer thicknesses of the elements. By choosing the layer thicknesses below the critical distance, low-temperature annealing will produce a series of amorphous alloys. Further annealing of these samples at higher temperatures results in crystallization. Crystallization temperature and the compound crystallized are then determined and the results compared with that expected for the various compositions from the equilibrium phase diagram. The results obtained from this type of investigation in the iron–silicon and the iron–aluminum system are representative and are presented next.

Crystallization of Amorphous Iron–Silicon Alloys

The iron-silicon phase diagram [9], shown in Figure 3, contains 4 binary compounds: $FeSi_2$, FeSi, Fe_5Si_3, and Fe_3Si. Of these, $FeSi_2$, FeSi, and Fe_3Si are all stable at low temperatures, while Fe_5Si_3 is only thermodynamically stable between

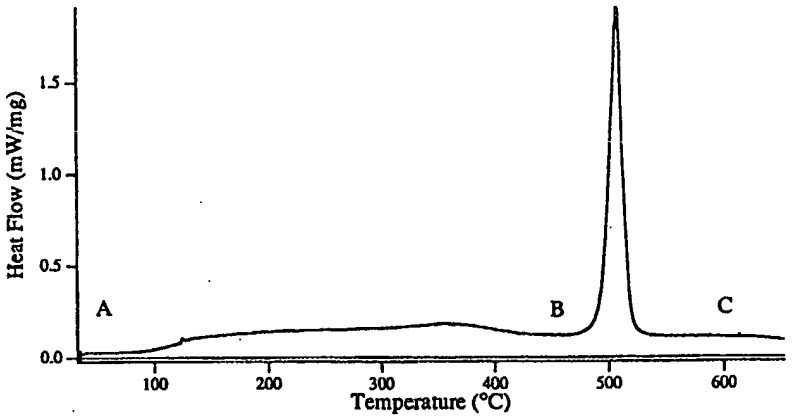

Figure 42. Heat flow as a function of temperature obtained for a layered composite of relative composition 1/2 iron/silicon. The upper curve was obtained by heating the sample at 10°C/min and subtracting a subsequent run on the same sample obtained under identical conditions. The baseline is the difference between the heat flow of the second and third heating of the same sample. At the points labeled A–C, diffraction data were collected and the diffraction patterns obtained are presented in Figure 43.

825° and 1060°C. The results from five representative superlattices are discussed below, four of which correspond in stoichiometry to these four compounds while the fifth's stoichiometry was two iron per silicon atom, corresponding to a eutectic composition in the phase diagram. In all these samples, as deposited there were no diffraction features at high angles, indicating that the layers are amorphous with respect to X-ray diffraction.

The irreversible solid state reactions occurring in the multilayer composites as temperature is raised were studied using differential scanning calorimetry. Figure 42 contains the DSC data for a sample of relative composition one iron per two silicon, which is representative of the data collected from all the samples. There is a broad exotherm with an onset temperature of 80°C continuing up to the sharp exotherm at 460°C. The broad exotherm is caused by interdiffusion of the iron and silicon, as confirmed by X-ray diffraction experiments in the temperature range 25°–340°C and discussed earlier (see Figs. 27–29). Also, a sample heated to 300°C and subsequently cooled was still X-ray amorphous (Fig. 43). Diffraction data collected after heating past the 460°C sharp exotherm identify the sample as crystalline $FeSi_2$ (Fig. 43). The DSC experiments combined with the temperature-dependent X-ray diffraction studies clearly indicate that the mixing of the elements has been separated from the crystallization of a binary phase.

The major features of the DSC data are summarized in Table 1 for all the samples studied. The onset of diffusion is found to be independent of composition. The

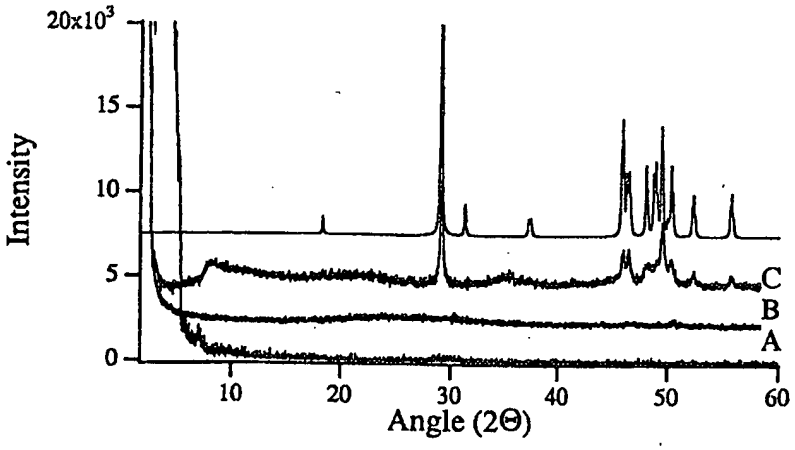

Figure 43. Diffraction data obtained on the iron–silicon superlattice at the temperatures indicated in Figure 42. The diffraction lines present at high angles in the scan taken at 600°C are those expected for $FeSi_2$. The upper curve is data obtained from the JCPDS diffraction files for a sample of crystalline $FeSi_2$. The curves are offset vertically for clarity.

diffusion onset is a measure of the activation energy for diffusion, which depends on the structure of the iron–silicon interface. The structure of the interface is a function of deposition conditions and should not be influenced by the overall stoichiometry of the film. Since deposition conditions were constant from sample to sample, the interface structure and therefore the diffusion onset should be composition independent.

The heat evolved in the formation of an amorphous alloy from a modulated composite (ΔH_{mixing}) depends on composition. This evolved heat results from the formation of iron–silicon bonds and therefore depends on the strength as well as the number of bonds in the amorphous alloy. The total number of iron–silicon bonds will be a minimum for compositions which are furthest from equimolar concentration. The smallest ΔH_{mixing} was found for samples with an iron–silicon ratio of 1 to 2 and 3 to 1, respectively. Experimentally, ΔH_{mixing} is larger for compositions closer to an equimolar ratio.

In addition to the broad, low-temperature, diffusion exotherm, all the samples except the eutectic composition show a sharp exotherm. Before this exotherm, the samples are still X-ray amorphous. Diffraction data collected after these exotherms clearly indicate that the phase which crystallized was closest in composition to the amorphous alloy. Table 2 contains the high-angle diffraction data and compares it with that previously reported for crystalline iron silicides. Excellent agreement is found between the observed and previously reported peak positions.

Table 1. Summary of Thermodynamic Data from Iron–Silicon Multilayers

Iron to Silicon Ratio	Diffusion Onset Temperature (°C)	Observed ΔH_{mixing}[a] (kJ/mole atom)	Observed $\Delta H_{crystallization}$[a] (kJ/mole atom)	Observed ΔH_{total}[a] (kJ/mole atom)	Literature Values $\Delta H_{formation}$ (kJ/mole atom)	Crystallization Onset Temperature (°C)
1:2	80	–20 (4)	–8 (1)	–28 (4)	–30.6 [44]	485
1:1	80	–22 (4)	–4 (0.5)	–26 (4)	–39.3 [45]	290
5:3	80	–30 (4)	–1 (0.3)	–31 (4)	—	455
2:1	80	–37 (4)	—	–37 (4)	—	—
3:1	80	–15 (4)	–1 (0.3)	–16 (4)	–25.8 [46]	540

Note: [a]Values in parentheses are the estimated error bars in the measurement due to the change in the heat capacity of the sample on crystallization

Table 2. Crystallographic Data for the Iron Silicides

Compound	*Observed d-spacing*	*Observed Intensities*	*Calculated d-spacing*	*Calculated Intensities*
$FeSi_2$	3.061	100	3.070	100
	3.051	100	3.060	100
	—	—	2.851	20
	—	—	2.412	10
	—	—	2.400	10
	1.998	43	1.980	50
	1.976	42	1.975	50
	1.956	34	1.960	40
	1.876	46	1.950	40
	—	—	1.892	50
	—	—	1.867	40
	—	—	1.860	40
	1.839	68	1.842	80
	1.817	5	1.822	10
	1.812	19	1.811	50
	1.748	16	1.751	20
	1.741	14	1.746	20
	1.643	20	—	—
FeSi	3.164	8	3.173	22
	2.586	9	2.590	13
	2.236	8	2.243	8
	2.006	100	2.007	100
	1.831	34	1.832	48
	—	—	1.587	1
	1.494	2	1.495	3
	—	—	1.419	3
	1.352	7	1.353	8
	1.293	2	1.295	3
	1.242	3	1.244	4
	1.199	13	1.199	20
Fe_5Si_3	—	—	3.350	10
	—	—	2.920	10
	—	—	2.740	10
	—	—	2.350	20
	—	—	2.210	60
	2.001	100	2.000	100
	—	—	1.940	80
	—	—	1.920	80
	1.832	12	1.830	10
	—	—	1.375	80
	—	—	1.620	10
	—	—	1.590	40
	—	—	1.530	10
	—	—	1.460	30
	—	—	1.375	50
	—	—	1.330	20
	—	—	1.291	10
	1.277	9	1.282	80
	—	—	1.244	50
Fe_3Si	3.274	1	3.250	40
	2.832	1	2.830	40
	2.007	100	1.990	100
	1.711	3	1.700	40
	—	—	1.620	20
	1.418	15	1.410	100
	1.277	3	—	—

Heats of crystallization of the binary silicides from the amorphous alloys are summarized in Table 1. These ($\Delta H_{crystallization}$) reflect the differences in structure (bond lengths and angles) between the amorphous and crystalline states. The largest heat of crystallization was found for the most ionic of the iron silicides, $FeSi_2$. The more metal-rich binary silicides have structures consistent with metallic bonding [106] and evolve less heat on crystallization, consistent with the less directional nature of the metallic bonding. The small heat of crystallization for Fe_3Si reflects the large amount of disorder in the structure, as reflected by its stability over a broad range of composition. The small heat of crystallization observed for Fe_5Si_3 may also result from its metastability at the temperature at which it nucleated.

The total heat evolved in the formation of each phase is the sum of the energy of mixing and the energy evolved during crystallization. This total heat evolved during the heat treatment of these films is compared with published values for the heats of formation of the crystalline compounds determined via other techniques in Table 1 [107–109]. Our values are consistently less than these published values as a result of the mixing which occurs during deposition to form our initial multilayer composites.

Table 1 also contains the crystallization temperature of the different compounds from their respective amorphous films. *Crystallization of iron silicides from an amorphous composite clearly depends on the composition of the amorphous alloy.* This includes the crystallization of an amorphous alloy with an iron/silicon ratio of 5:3 to the crystalline phase Fe_5Si_3 at a temperature of 500°C. This demonstrates that *nucleation is the controlling factor in the evolution of the amorphous alloy* because Fe_5Si_3 is thermodynamically unstable with respect to a mixture of Fe_3Si and FeSi at temperatures below 825°C. FeSi, the first phase expected to form from the first phase rule, has the lowest crystallization temperature. It is the easiest binary silicide to nucleate from an amorphous alloy, agreeing with previous literature reports, which stated that FeSi nucleates at temperatures between 240° and 400°C [110,111]. The other crystalline iron silicides all crystallize below 600°C from the amorphous intermediate corresponding to their respective stoichiometry.

All the crystalline iron silicide structures are of similar complexity, containing from 6 to 12 atoms per crystallographic unit cell. To test the limits of stoichiometric control of nucleation, we investigated the iron–aluminum system. Iron aluminides are much more "metallic" in their bonding, suggesting a smaller difference in structure and energetics between the amorphous intermediates and the crystalline compounds. In addition, the complexity of the crystalline compounds varies considerably.

7.3. Lessons Learned from the Iron–Aluminum System

The iron–aluminum phase diagram [9] contains as many as seven binary compounds including $FeAl_3$, Fe_2Al_5, $FeAl_2$, FeAl, and Fe_3Al. All five of these compounds are thermodynamically stable at low temperatures. The crystalline structures of these compounds vary considerably in their complexity. FeAl has an

extremely simple crystal structure containing only two atoms per unit cell while $FeAl_3$, $FeAl_2$, Fe_2Al_5, and Fe_3Al have considerably more complex crystal structures containing 102, 18, 14, and 16 atoms per crystallographic unit, respectively. In addition to the complexity of their unit cells, these compounds vary considerably in their phase width, with FeAl being stable over a considerable composition range while the other compounds have significantly narrower phase fields.

In general, nucleation temperatures have been found to be related to the complexity of the nucleating structure, with more complex structures having a larger nucleation volume and higher barriers to nucleation. Phase width is also likely to be an important factor, as it indicates the stability of structure with respect to defects. The simple crystal structure of FeAl combined with its large phase field makes avoiding the nucleation of FeAl a challenging test for superlattice reactants.

Toward this end, a series of superlattices was prepared with bilayer thicknesses ranging from 17 to 130 Å and stoichiometries between FeAl and $FeAl_2$. In all these samples, there were diffraction features at high angles, indicating that at least part of the layers were crystalline as deposited. In samples containing thick aluminum layers (greater than approximately 30 Å), diffraction peaks consistent with crystalline aluminum were observed. For samples with the thinner bilayer repeat units (less than approximately 50 Å), a high-angle diffraction peak consistent with crystalline FeAl was observed. The low-angle diffraction patterns were consistent with significant interdiffusion on deposition, showing a rapid decrease in diffraction intensity with diffraction order.

Combined DSC and high-angle X-ray diffraction studies on all the samples prepared suggest that FeAl is always the first binary compound which forms during annealing. Interestingly, the second compound which forms is Fe_2Al_5, which has the next widest phase field in the iron–aluminum phase diagram. This suggests that phase width may have a significant effect on nucleation temperatures.

The iron–aluminum system demonstrates the importance of avoiding crystallization until after a homogeneous, amorphous state has been obtained. The heterogeneous nucleation of FeAl in iron aluminum superlattices prevents any control of the reaction. This is in contrast to the iron–silicon alloys discussed in the previous section, where a homogeneous amorphous state is reached. In iron–silicon, composition of the amorphous reaction intermediate controls crystallization.

In a ternary system, the challenge is to crystallize the desired ternary compound without the formation of crystalline binary compounds as reaction intermediates. The iron–aluminum system highlights the potential importance of layer sequence in the synthesis of a ternary compound, as a complex layer sequence such as ABCB avoids direct reaction between A and C. This type of layer sequence prevents the crystallization of simple binary compounds typified by FeAl. These ideas are extended in the next section.

7.4. Direct F rmation f a Ternary Compound from a Superlattice Reactant

The results of Sections 7.1–7.3 suggest a rational synthetic sequence to a ternary compound which does not involve binary compounds as reaction intermediates. This sequence starts with determining the critical diffusion distances in each of the binary diffusion couples. The design of a ternary superlattice is then based on this information. If the binary reaction information is transferable to the ternary system, a system layered below the smallest critical distance should yield an amorphous intermediate on low-temperature annealing. The composition of the ternary amorphous alloy could then be used to favor the crystallization of a ternary product over nucleation of a binary, since the ternary component must first diffuse out of the nucleating volume before a binary compound can crystallize.

Ternary superlattices also have an additional experimental variable not available in binary systems—the order of the elemental layers. Complex layer sequences can potentially be used to control the diffusion process. As a simple example, the reaction of a composite based on the repetition of the layer sequence ABC involves the simultaneous reaction at AB, BC, and AC interfaces while the reaction of a composite based on the repetition of the layer sequence ABCB involves initial reaction of only AB and BC interfaces. Thus, the repeat unit of a superlattice composite can be used as an experimental variable to investigate and control solid state reactions.

The copper–molybdenum–selenium system was chosen for our initial investigation to take advantage of the background data available on the binary molybdenum–selenium system. The goal was to prepare the compound $Cu_2Mo_6Se_8$ directly from an amorphous intermediate.

Direct Crystallization of $Cu_2Mo_6Se_8$ from Ternary Copper–Molybdenum–Selenium Superlattices

Superlattice samples corresponding to the stoichiometry of the desired ternary compound, $Cu_2Mo_6Se_8$, were prepared both above and below the critical thicknesses determined for the binary systems Cu–Mo, Cu–Se, and Mo–Se. Differential scanning calorimetry data and X-ray diffraction data were collected as a function of heating temperature and time to follow the evolution of the composites.

Three thin ternary samples containing 10 Å of copper, 30 Å of molybdenum, and 82 Å of selenium were prepared to study the reaction of a superlattice modulated above the critical thickness found for the molybdenum–selenium system. Differential scanning calorimetry data obtained on one of these samples, shown in Figure 44, contain two low-temperature exotherms at 100° and 200°C and a broad exotherm centered at 500°C in addition to an endotherm at 725°C. Diffraction data collected after annealing the samples to various temperatures indicated in Figure 44 are shown in Figure 45. Similarities with the molybdenum–selenium studies imply that the lowest temperature exotherm corresponds to the interdiffusion of

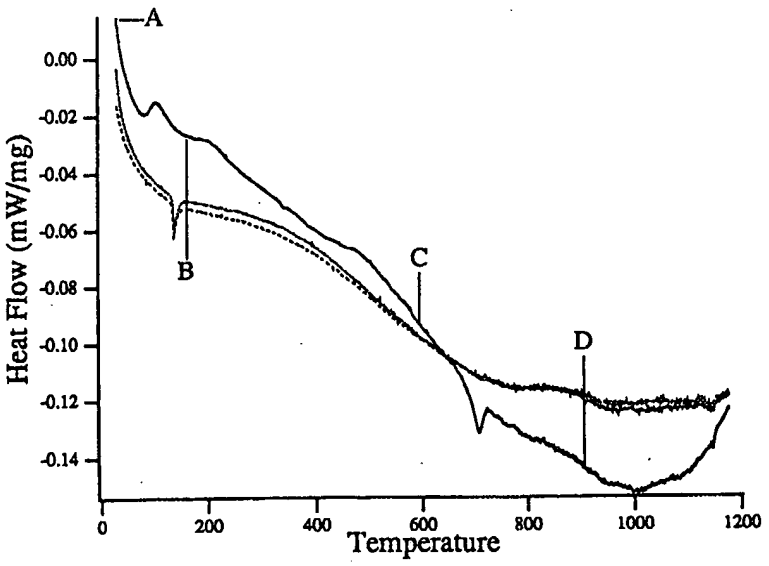

Figure 44. Thermograms obtained for a ternary copper–molybdenum–selenium superlattice consisting of a repeating unit containing 10 Å of copper, 30 Å of molybdenum, and 82 Å of selenium. The upper curve is the first thermogram and contains the irreversible changes in the sample as it is initially heated. The lower curve is the second thermogram and is an effective baseline. At the points labeled A–D, diffraction data were collected and the diffraction patterns obtained are presented in Figure 45.

the molybdenum and selenium layers. The second exotherm is due to the nucleation of the binary compound $MoSe_2$, and the broad exotherm centered at 500°C corresponds to growth of $MoSe_2$ crystallites. $MoSe_2$ was the lone crystalline component found at 600°C. The ternary product, $Cu_2Mo_6Se_8$, was observed only after the endotherm at 725°C, suggesting that this endotherm is due to the reaction of crystalline $MoSe_2$ with the remaining amorphous part of the superlattice to form the ternary product, $Cu_2Mo_6Se_8$. The reaction of these samples is similar to that found in bulk solid state reactions, in that ternary products are formed from the reaction of crystalline binary compounds generated as reaction intermediates.

To explore the effect of layer thickness, two ultrathin-film ternary samples were prepared with a repeating layer sequence of 3 Å of copper, 9 Å of molybdenum, and 25 Å of selenium. The layer thicknesses in these samples are less than the shortest critical distance found for any of the component binary systems. Differential scanning calorimetry data obtained on these samples differ noticeably from

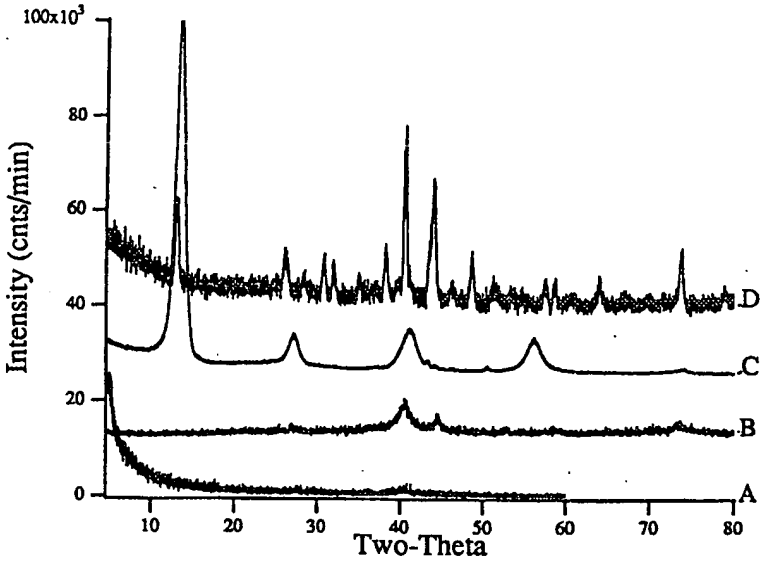

Figure 45. Diffraction data obtained for a ternary copper–molybdenum–selenium superlattice consisting of a repeating unit containing 10 Å of copper, 30 Å of molybdenum , and 82 Å of selenium at the temperatures indicated on Figure 44. The curves are offset vertically for clarity.

those observed for the thicker samples, as shown in Figure 46. Three broad exotherms are observed, the lowest temperature one occurring between 150° and 300°C, the second between 600° and 800°C, and the third between 850° and 1100°C. The endothermic transition observed at 725°C in the thicker samples is not found for these ultra-thin samples.

Diffraction data collected as a function of temperature, shown in Figure 47, confirm that thinner layers changed the intermediates of the reaction. As deposited, the superlattice is layered and X-ray amorphous. After heating to 170°C, the sample has begun to interdiffuse, and there are two small diffraction peaks in the high-angle diffraction data, suggesting that something has begun to crystallize. The position of these diffraction peaks does not coincide with that expected for any known binary compound. The only change in the diffraction pattern during extended annealing of the sample below 500°C is the disappearance of the low-angle Bragg diffraction peaks as the elemental layers interdiffuse. The two small diffraction maxima evident in the high-angle diffraction scan at 170°C become less evident as a result of this annealing. The diffraction pattern of the sample obtained after annealing at 600°C indicates that the ternary compound has begun to crystallize, suggesting that the exotherm between 600° and 800°C results from this crystallization. The diffraction patterns collected between 600° and 1200°C show the

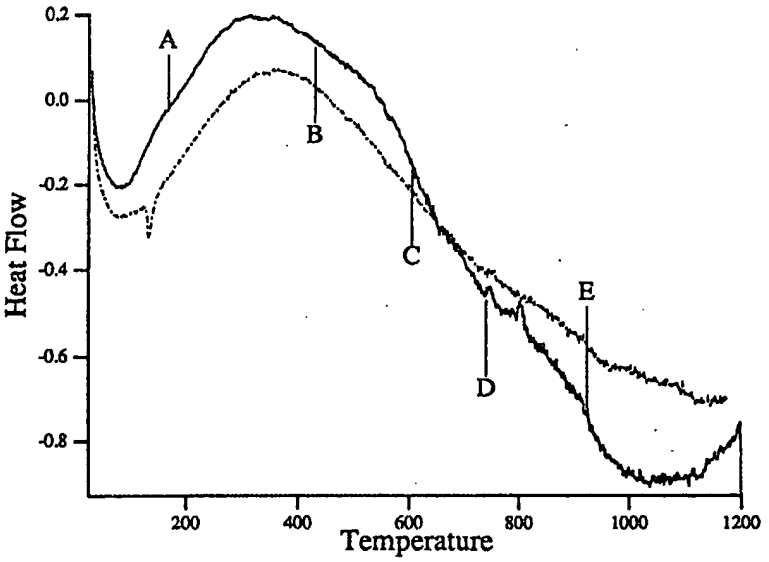

Figure 46. Thermograms obtained for a ternary copper–molybdenum–selenium superlattice consisting of a repeating unit containing 3 Å of copper, 9 Å of molybdenum, and 25 Å of selenium. The upper curve is the first thermogram and contains the irreversible changes in the sample as it is initially heated. The lower curve is the second thermogram and is an effective baseline. At the points labeled A–D, diffraction data were collected and the diffraction patterns obtained are presented in Figure 47.

gradual development of the full diffraction pattern of the ternary compound, with no evidence for the formation of crystalline, binary intermediates. The gradual improvement in the crystallinity of the ternary product is clearly evident by smooth increase in the particle sizes obtained from the diffraction line widths.

The same final crystalline product was obtained from both the thin and ultrathin superlattice reactants. The lattice parameters are consistent between the samples, indicating the ability to control the stoichiometry of the initial superlattice reactants. Further evidence for the consistency of the stoichiometry of the samples comes from the background DSC scans obtained for both samples, which show sharp, reversible endothermic transitions at 150°C. This endothermic transition results from an order–disorder transition of the copper atoms and has been found to be sensitive to the copper stoichiometry.

Although the same product was formed from superlattices in both thickness regimes, the reaction sequences were completely different. The reaction sequence observed for the thin ternary superlattice was similar to that expected for a "bulk"

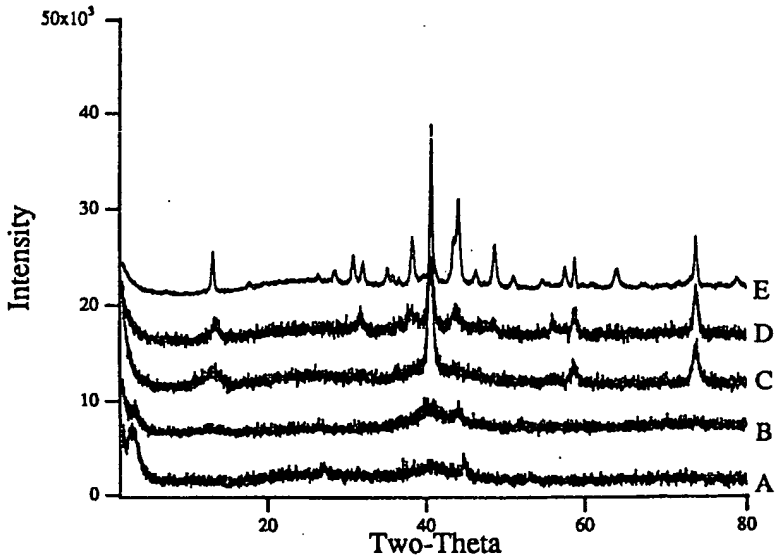

Figure 47. Diffraction data obtained for a ternary copper–molybdenum–selenium superlattice consisting of a repeating unit containing 3 Å of copper, 9 Å of molybdenum and 25 Å of selenium at the temperatures indicated in Figure 46. The curves are offset vertically for clarity.

reaction. In a bulk reaction, one reactant typically becomes mobile before the others and reacts with the stationary elements to form binary compounds. In the bulk reaction between copper, molybdenum, and selenium, selenium is the first element to become mobile and reacts with the metals to form binary compounds. The thin superlattice initially formed $MoSe_2$ at the molybdenum–selenium interfaces, as expected from our earlier investigation of the effect of layer thickness on the reaction sequence of binary molybdenum–selenium superlattices.

In the ultrathin sample, the initially layered superlattice was found to slowly interdiffuse below 550°C. After the initial stages of the exotherm beginning at 550°C, $Cu_xMo_6Se_8$ was found to have nucleated directly. There is no evidence for the formation of any crystalline, reaction intermediates.

This study generalizes and extends earlier conclusions obtained from the study of binary superlattice reactants to ternary systems: layer thickness is an important reaction parameter in controlling the reaction mechanism, and the composition of any resulting homogeneous, amorphous intermediate can be effective in directing crystallization. The results of this study also suggest that critical distance information obtained from the study of binary superlattice reactants is an effective starting point for the investigation of ternary superlattices. This permits a rational approach to the design of a ternary superlattice reactant.

8. FUTURE RESEARCH DIRECTIONS

Our research thus far has focused on the development of a new approach to solid state synthesis using superlattices as unique and tailorable reactants. The studies have addressed the preparation of known compounds in established phase diagrams via desired reaction intermediates to determine the capabilities and limitations of superlattices as reactants. The ability to tailor the structure of superlattices on an ångstom level has opened new reaction pathways and provided the capability of controlling the reaction pathway taken by the superlattice.

The next step in demonstrating the capability of these unique reactants is to apply this approach to the preparation of new compounds. An obvious initial area in which to apply this methodology is the synthesis of new ternary compounds which are metastable with respect to binary constituents. This is a natural extension of the copper–molybdenum–selenium investigation and preliminary work in this direction has already yielded very encouraging results.

Several other research directions are also suggested by the unique capabilities of superlattice reactants which are not as synthetically focused. These research directions are described in the following several paragraphs.

Changes in the low-angle diffraction pattern with annealing temperature and time in principle allow one to follow solid state reactions at buried interfaces on an ångstrom level, and should permit a detailed description of how elements or compounds react in the solid state. Progress in this area is tied to an improvement in the ability to interpret the low-angle diffraction patterns and extract elemental composition profiles from these data. The ability to follow interfacial reactions has considerable practical importance in addition to the scientific significance. Many physical phenomena are affected by interfacial structure and/or interfacial reactions. An example is found in the physical properties of composite materials which are often dominated by interfacial phases formed by the reaction of the individual components of the composite. A detailed knowledge of the structural and chemical development of the interfacial regions is crucial to improving performance in a rational manner.

The ability to prepare amorphous intermediates makes superlattice reactants an ideal way to explore low-temperature phase diagrams. Traditionally, phase diagrams have been explored by slowly cooling high-temperature melts. It is extremely difficult to form compounds which are stable only at low temperatures by this procedure as compounds formed at high temperatures must subsequently react. This reaction involves large diffusion distances, and since solid state diffusion is very limited at low temperatures, there is no kinetic access to compounds only stable at low temperatures. Superlattice reactants permit phase diagrams to be explored from the bottom up, from low temperatures to high, via the formation of a metastable, amorphous reaction intermediate. The composition of this amorphous intermediate is then used as a probe to search for compounds only stable at low temperatures.

The ability to form amorphous intermediates also presents the opportunity to study nucleation phenomenon in the solid state. Solid state nucleation is a complex process which has been extensively investigated only in glass-forming systems such as silicates. The ability to form amorphous intermediates within systems with widely varying structures and bonding tendencies can be used to expand on these initial studies. It will be crucial to separate the variables affecting the nucleation process as much as possible. The studies described in this chapter have been performed on free-standing samples to eliminate substrate effects. Temperature and composition are the only variables which have been explored systematically. Since the nucleation process often involves a volume change, an obvious additional parameter to explore is hydrostatic pressure. Changes in nucleation temperature with pressure can then be used to determine a "volume of activation" for the nucleation event.

The substrate can affect the nucleation process in at least two ways, by providing nucleation sites or by producing large internal stresses in the superlattice film on annealing. The importance of internal stress can be experimentally probed by depositing upon substrates which are prestressed. The idea is to stress the substrate, causing it to bend. By depositing upon the concave surface and then unstressing the substrate, a longitudinal external stress is imposed on the film. By depositing upon the convex surface and then unstressing the substrate, a compressive external stress is imposed on the film. By varying the initial stress imposed on the substrate, the effect of external stress upon nucleation can be systematically explored. Changes in nucleation temperature with stress could then be used as an additional variable when using superlattice reactants to prepare new materials.

It is also well-known that substrates provide nucleation sites, resulting in epitaxial growth of the nucleated phase upon the substrate. This process could be exploited to direct the nucleation of the amorphous intermediate to a desired structure, although one of the major experimental limitations of epitaxial growth has historically been the lack of high-quality substrate material of the desired structure.

Nucleation can also be controlled by the addition of impurities to act as nucleation centers. This phenomenon, referred to as seeding, is potentially a very powerful way to control nucleation when using superlattices as reactants. The basic idea is to take advantage of the limited diffusion rates within the low-temperature reactions of superlattices, as shown in Figure 48. A superlattice is prepared containing layers of the elements designed to produce an amorphous intermediate for the desired compound. On top of this superlattice, a limited amount of a second set of elements is then deposited. The composition and structure of those layers are chosen so as to produce an amorphous intermediate which will crystallize into a compound, isostructural to the desired product. Finally, on top of these layers, more of the original superlattice is deposited. This superlattice composite is then heated to interdiffuse the layers, resulting in a sandwich of amorphous material still segregated between the first, second, and third depositions due to limitations in diffusion rates at the low annealing temperatures. Ideally, the middle layer then crystallizes, causing the top and bottom layers to crystallize into the desired

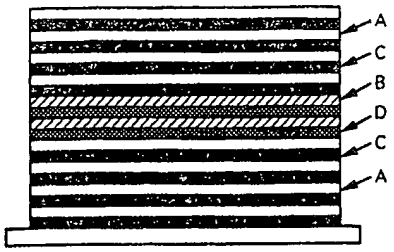

Figure 48. Portion of an ultra-thin-film superlattice designed such that the middle layers of the resulting amorphous composite "seed" the crystallization of the desired compound. In an actual sample the number of A and C layers would greatly exceed the number of B and D layers.

isostructural compound. Preliminary investigations in our laboratory using this approach have been extremely encouraging.

Controlling nucleation in the amorphous intermediate should also permit formation of single-crystal films of desired compounds. One route to single crystal films is adapting a "trick" used to grow single crystals from melts, in which a polycrystalline seed is initially used to begin the growth process. The growing polycrystalline boule is then thinned down to a very narrow neck such that only one of the growing crystallites has the correct orientation. After this necking procedure, the remaining growth of the boule is a single crystal from the one crystallite which grew through the neck. The adaptation of this approach to our thin-film systems is shown in Figure 49 and involves a lithographically patterned substrate which

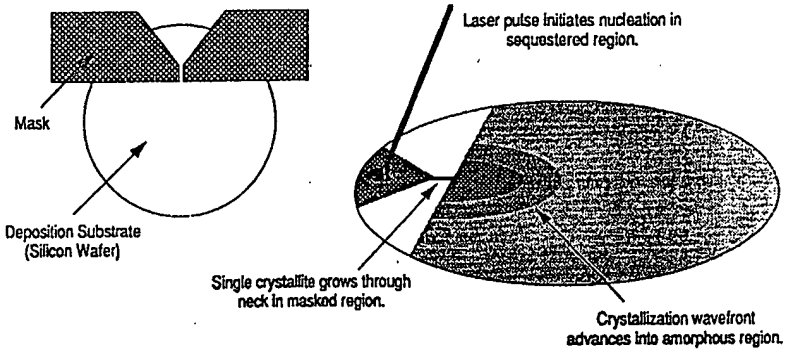

Figure 49. Proposed procedure to prepare single crystal films via patterning of the deposited region followed by localized heating in one of the sequestered regions. Only one crystallite will have the correct orientation to grow through the necked region of the amorphous film.

Figure 50. Proposed "designer compound" consisting of a superstructure of $MoSe_2$ and $NbSe_2$.

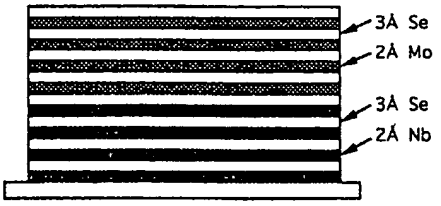

Figure 51. Portion of the proposed "superlattice of superlattices" designed to form the compositionally modulated compound shown in Figure 50.

divides the amorphous film into two regions separated by a narrow neck. A heat pulse in one region results in multiple nucleation events, but hopefully only one of the growing crystals will survive through the neck region. This growing crystallite then acts as the lone nucleation site for the second region. Volume changes during crystallization will probably set an upper size limit on the single crystal area.

Superlattice reactants should also permit the preparation of "designer compounds" consisting of a chemically modulated crystalline structure, as shown in Figure 50. The synthesis of such a compound again takes advantage of the limited long-range diffusion which occurs during the low-temperature annealing of the initial superlattice. The chemically modulated structure shown in Figure 50 is prepared from an intergrown superlattice of superlattices as shown in Figure 51.

9. SUMMARY

In this chapter we have presented the progress made to date on the development of superlattices as unique reactants. The use of superlattices as reactants results in

- easy control and optimization of diffusion distances;
- control of the diffusion process via manipulation of the layer sequence; and

- low-temperature interdiffusion due to low atomic densities and large number of defects in the as-deposited multilayers.

The ordered arrangement of the layers and interfaces in a superlattice produces a low-angle diffraction pattern. This superlattice diffraction pattern permits

- the detailed structural characterization of the starting reactant;
- the interfacial composition profiles to be determined;
- the interfacial roughness to be quantified; and
- the interdiffusion process to be followed on an ångstom level in a quantitative manner by measuring the decay of diffraction pattern with time and temperature.

The high densities of the interfaces within a superlattice permit

- the calorimetric determination of the heat of interdiffusion and crystallization.

The studies presented in Section 7 suggest that the above characteristics of superlattice reactants permit a rational approach to the formation of new compounds. In particular,

- an amorphous intermediate can be formed by tailoring the layer thicknesses and deposition order of the layers within the initial superlattice reactant;
- the formation of the amorphous reaction intermediate is monitored by calorimetry, low-angle and high-angle X-ray diffraction;
- nucleation is a rate-limiting step in forming a crystalline compound from an amorphous intermediate made by the low-temperature interdiffusion of an ultrathin superlattice;
- nucleation temperatures can be controlled by the composition of the amorphous intermediate;
- metastable, binary compounds can be formed under conditions where they are unstable; and
- ternary compounds can be prepared without the formation of crystalline binary compounds as reaction intermediates.

These capabilities have opened up new avenues of solid state research.

ACKNOWLEDGMENTS

This work was supported by a Young Investigator Award from the Office of Naval Research (N00014-87-K-0543) and the continuation grant (N0014-91-J-1288). Support by the National Science Foundation (DMR-8704652, DMR 9213352); the donors of the Petroleum Research Fund administered by the American Chemical Society; the University of Oregon; and the U.S. Department of Education Graduate Assistance in Areas of Need Program for (TN, LF, and CG) is gratefully acknowledged.

REFERENCES

1. Sagawa, M.; Fujimura, S.; Togawa, N.; Yamamoto, H.; Matsura, Y. *J. Appl. Phys.* **1984**, *55*, 2083.
2. Croat, J. J.; Herbst, J. F.; Lee, R. W.; Pinkerton, F. E. *J. Appl. Phys.* **1984**, *55*, 2078.
3. Sleight, A. W. *Science* **1988**, *242*, 1519.
4. DiSalvo, F. J. In *Advancing Materials Research*; P. A. Psaras and H. D. Langford, Eds.; National Academy Press: Washington, DC, 1987; pp. 161–176.
5. West, A. R. *Solid State Chemistry and its Applications*; John Wiley & Sons: New York, 1989.
6. Johnson, D. C.; Tarascon, J. M.; Sienko, M. J. *Inorganic Chemistry* **1985**, *24*, 2808–2812.
7. Corbett, J. D. In *Solid State Chemistry Techniques*; A. K. Cheetham and P. Day, Eds.; Clarendon Press: Oxford, 1987; pp. 2.
8. Brophy, J. H.; Rose, R. M.; Wulff, J. *The Structure and Properties of Materials*; 1964; Vol. 2, pp. 98–108.
9. *Binary Alloy Phase Diagrams*; 2d Ed.; Massalski, T. B.; Okamoto, H.; Subramanian, P. R.; Kacprzak, L., Eds.; ASM International: 1990; Vol. 3, pp. 2664–2665.
10. Kubaschewski, O.; Alcock, C. B. *Metalurgical Thermochemistry;* 5th Ed.; Pergamon Press: New York, 1979.
11. Herd, S.; Tu, K. N.; Ahn, K. Y. *Appl. Phys. Lett.* **1983**, *42*, 597.
12. Nava, F.; Psaras, P. A.; Takai, H.; Tu, K. N. *J. Appl. Phys.* **1986**, *59*, 2429–2438.
13. Gas, P.; d'Heurle, F. M.; LeGoues, F. K.; La Placa, S. J. *J. Appl. Phys.* **1986**, *59*, 3458–3466.
14. Coulman, B.; Chen, H. *J Appl. Phys.* **1986**, *59*, 3467–3474.
15. Canali, C.; Catellani, F.; Ottaviani, G.; Celotti, G. *J. Appl. Phys.* **1979**, *50*, 255–258.
16. Ziegler, E.; Lepetre, Y.; Schuller, I. K.; Spiller, E. In *Grazing Incidence Optics*; 1986; Vol. SPIE 640, pp. 145–148.
17. Bené, R. W. *Appl. Phys. Lett.* **1982**, *41*, 529–531.
18. Walser, R. M.; Bené, R. W. *Appl. Phys. Lett.* **1976**, *28*, 624–625.
19. Lau, S. S.; Feng, J. S. Y.; Olowolafe, J. O.; Nicolet, M. A. *Thin Solid Films* **1975**, *25*, 415–422.
20. Tsaur, B. Y.; Lau, S. S.; Mayer, J. W.; Nicolet, M.-A. *Appl. Phys. Lett.* **1981**, *38*, 922–924.
21. Schwarz, R. B.; Johnson, W. L. *Phys. Rev. Lett.* **1983**, *51*, 415–418.
22. Cotts, E. J.; Meng, W. J.; Johnson, W. L. *Phys. Rev. Lett.* **1986**, *57*, 2295–2298.
23. Clemens, B. M.; Sinclair, R. In *MRS Bulletin*; 1990; pp. 19–28.
24. Miedima, A. R.; Niessen, A. K. *Physica* **1982**, *114B*, 367–374.
25. Van der Kolk, G. J.; Miedema, A. R.; Niessen, A. K. *J. Less Common Metals* **1988**, *145*, 1–17.
26. Bormann, R.; Gartner, F.; Zoltzer, K. *J. Less Common Metals* **1988**, *145*, 19–29.
27. Saunders, N.; Miodownik, a. P. *J. Mater. Res.* **1986**, *1*, 38–46.
28. Gibbs, J. W. *Collected Works*; Yale University Press: New Haven, CT, 1948; Vol. 1, pp. 105–115, 252–258.
29. Gösele, U.; Tu, K. N. *J. Appl. Phys.* **1989**, *66*, 2619–2626.
30. Johnson, D. W., Jr. *Ceram. Bull.* **1981**, *60*, 221–224.
31. Horowitz, H. S.; Longo, J. M. *Mater. Res. Bull.* **1978**, *13*, 1359–1369.
32. Gopalakrishnan, J. *Proc. Indian. Acad. Sci., Chem. Sci.* **1984**, *93*, 421–432.
33. Rao, C. N. R.; Gopalakrishnan, J.; Vidyasgar, K.; Ganguli, A. K.; Ramanan, A.; Ganapathi, L. *J. Mater. Res.* **1986**, *1*, 280–294.
34. Matijevic, E. *Ann. Rev. Mater. Sci.* **1985**, *15*, 483–516.
35. Barrer, R. M. *Hydrothermal Synthesis of Zeolites*; Academic Press: New York, 1982.
36. Rouxel, J.; Meerschaut, A.; Gressier, P. *Synth. Met.* **1989**, *34*, 597–607.
37. Gerand, B.; Nowogrocki, G.; Guenot, J.; Figlarz, M. *J. Solid State Chem.* **1979**, *29*, 429–434.
38. Marchand, R.; Brohan, L.; Tournoux, M. *Mater. Res. Bull.* **1980**, *15*, 1129–1133.
39. Glass ceramics are formed by the controlled crystallization of a glass such that many nuclei are formed. The resultant fine-grained ceramics have very high strength and adjustable thermal expansion coefficients.

40. Beck, H.; Güntherodt, H.-J. In *Glassy Metals I: Ionic Structure, Electronic Transport, and Crystallization*; H. Beck and H.-J. Güntherodt, Eds.; Springer-Verlag: New York, 1981; Vol. 46; pp. 1–17.
41. Klement, W.; Willens, R. H.; Duwez, P. *Nature* **1960**, *187*, 869.
42. Duhaj, P.; Sladek, V.; Mrafko, P. *J. Non-Cryst. Solids* **1973**, *13*, 179–182.
43. Koster, U.; Herold, U. In *Glassy Metals I: Ionic Structure, Electronic Transport, and Crystallization*; H. Beck and H.-J. Güntherodt, Eds.; Springer-Verlag: New York, 1981; Vol. 46; pp. 225–259.
44. Calka, a.; Radlinski, A. P. *Acta Met.* **1987**, *35*, 1823–1829.
45. Buschow, K. H. J.; Beekmans, N. M. *Solid State Commun.* **1980**, *35*, 233–236.
46. Buschow, K. H. J. *Solid State Commun.* **1982**, *43*, 171–174.
47. Barbour, J. C.; Nastasi, M.; Mayer, J. W. *Appl. Phys. Lett.* **1986**, *48*, 517–519.
48. Barbour, J. C.; deReus, R.; Denier van der Gon, A. W.; Saris, F. W. *J. Mater. Res.* **1987**, *2*, 168–172.
49. Loeff, P. I.; Weeber, A. W.; Miedema, A. R. *J. Less Common Metals* **1988**, *140*, 299–305.
50. De Reus, R.; Saris, F. W. *Mater. Lett.* **1990**, *9*, 487–493.
51. Mayer, J. W.; Poate, J. M.; Tu, K.-N. *Science* **1975**, *190*, 228–234.
52. Webb, R. J.; Goldman, A. M. *J. Vac. Sci. Technol. a* **1985**, *3*, 1907–1912.
53. Nastasi, M.; Hung, L. S.; Johnson, H. H.; Mayer, J. W.; Williams, J. M. *J. Appl. Phys.* **1985**, *57*, 1050–1054.
54. Fister, L.; Li, X. M.; Novet, T.; McConnell, J.; Johnson, D. C. in preparation.
55. Barbee, T. W., Jr. *MRS Bull.* **1990**, *15*, 37–44.
56. Bartels, W. J.; Hornstra, J.; Lobeek, D. J. W. *Acta Cryst* **1986**, *A42*, 539–545.
57. Chauvineau, J. P. *Rev. Phys. Appl.* **1988**, *23*, 1645–1652.
58. Falco, C. M. In *Physics, Fabrication, and Applications of Multilayered Structures*; P. Dhez and C. Weisbuch, Eds.; Plenum Press: New York, 1988; Vol. 182; pp. 3–15.
59. Gilfrich, J. V.; Brown, D. B.; Rosen, D. In *Multilayer Structures and Laboratory X-Ray Laser Research*, 1986; Vol. SPIE 688; pp. 115–121.
60. James, R. W. *The Optical Principles of the Diffraction of X-Rays*; Ox Bow Press: Woodbridge, CT, 1982, pp. 172–173.
61. Knight, L. V.; Thorne, J. M.; Toor, A.; Barbee, T. W., Jr. *Rev. Phys. Appl.* **1988**, *23*, 1631–1644.
62. Lim, G.; Parrish, W.; Ortiz, C.; Bellotto, M.; Hart, M. *J. Mater. Res.* **1987**, *2*, 471–477.
63. McWhan, D. B. In *Synthetic Modulated Structures*; Chang, L. C. and Giessen, B. C., Eds.; Academic Press: New York, 1985; pp. 43–74.
64. Narayanamurti, V. *Science* **1987**, *235*, 1023–1028.
65. Névot, L.; Croce, P. *Rev. Phys. Appl.* **1980**, *15*, 761–779.
66. Névot, L.; Pardo, B.; Corno, J. *Rev. Phys. Appl.* **1988**, *23*, 1675–1686.
67. Pardo, B.; Megademini, T.; André, J. M. *Rev. Phys. Appl.* **1988**, *23*, 1579–1597.
68. Rosenbluth, A. E.; Lee, P. *Appl. Phys. Lett.* **1982**, *40*, 466–468.
69. Rosenbluth, A. E. *Rev. Phys. Appl.* **1988**, *23*, 1599–1621.
70. Savage, D. E.; Kleiner, J.; Schimke, N.; Phang, Y.-H.; Jankowski, T.; Jacobs, J.; Kariotis, R.; Lagally, M. G. *J. Appl. Phys.* **1991**, *69*, 1411–1424.
71. Shaw, K. D.; Krieger, A. S. *Appl. Opt.* **1989**, *28*, 1052–1054.
72. Spiller, E. *Rev. Phys. Appl.* **1988**, *23*, 1687–1700.
73. Stearns, M. B. *Phys. Rev. B* **1988**, *38*, 8109–8113.
74. Spiller, E. In *Physics, Fabrication, and Applications of Multilayered Structures*; Dherz, D. and Weisbuch, C., Eds.; Plenum Press: New York, 1988; pp. 271–309.
75. Stearns, D. G. *J. Appl. Phys.* **1989**, *65*, 491–506.
76. Stearns, D. G.; Rosen, R. S.; Vernon, S. P. *J. Vac. Sci. Technol. A.* **1991**, *9*, 2662–2669.
77. Underwood, J. H.; Barbee, T. W., Jr. *Appl. Opt.* **1981**, *20*, 3027–3034.
78. Wood, J.; Grupido, N.; Hart, K.; Flessa, S.; Kadin, A.; Keem, J.; Ferris, D. *Mater. Res. Soc. Symp. Proc.* **1986**, *56*, 435–440.

79. Klug, H. P.; Alexander, L. E. *X-ray Diffraction Procedures for Polycrystalline and Amorphous Materials;* 2d Ed.; John Wiley & Sons: New York, 1974, pp. 100–102.
80. Ladd, M. F. C.; Palmer, R. A. *Structure Determination by X-ray Crystallography;* 1st Ed.; Plenum Press: New York, 1978; p. 393.
81. Woolfson, M. M. *An Introduction to X-ray Crystallography;* 1st Ed.; Cambridge University Press: New York, 1970; p. 380.
82. Tang, Z.; Xu, Z.; Kevan, S. D.; Novet, T.; Johnson, D. C. *Appl. Phys. Lett.* (submitted).
83. Xu, Z.; Tang, Z.; Kevan, S. D.; Novet, T.; Johnson, D. C. (in preparation).
84. Warren, B. E.; Averbach, B. L. *J. Appl. Phys.* **1950**, *21*, 595.
85. Carcia, P. F.; Li, Z. G. *J. Appl. Phys.* **1992**, *71*, 842–848.
86. Liu, J.; Cheng, Y.; Lewen, G. D.; Stearns, M. B. In *Materials Research Society*; Materials Research Society: Boston, MA, 1992; pp. 641–646.
87. Harmelin, M.; Jiansheng, J. *Thermochim. Acta* **1990**, *162*, 453.
88. Ranijmakers, I. J. M. M.; Reader, A. H.; Oosting, P. H. *J. Appl. Phys.* **1988**, *63*, 2790–2795.
89. Brasen, D.; Willens, R. H.; Nakahara, S.; Boone, T. *J. Appl. Phys.* **1986**, *60*, 3527–3531.
90. Holloway, K.; Sinclair, R. *J. of Appl. Phys.* **1987**, *61*, 1359–1364.
91. Greer, A. L.; Spaepen, F. In *Synthetic Modulated Structures*; L. C. Chang and B. C. Giessen, Eds.; Academic Press: New York, 1988; pp. 419–486.
92. DuMond, J.; Youtz, J. P. *J. Appl. Phys.* **1940**, *11*, 357–365.
93. Fleming, R. M.; McWhan, D. B.; Gossard, A. C.; Wiegmann, W.; Logan, R. A. *J. Appl. Phys.* **1980**, *51*, 357–363.
94. Murakami, M.; Segmüller, A.; Tu, K. N. In *Analytical Techniques for Thin Films*; K. N. Tu and R. Rosenberg, Eds.; Academic Press: New York, 1988; Vol. 27; pp. 201–248.
95. Novet, T.; McConnell, J. M.; Johnson, D. C. In *Materials Research Society*; Materials Research Society: Boston, MA, 1991; pp. 581–586.
96. Novet, T.; Johnson, D. C. *J. Am. Chem. Soc.* **1991**, *113*, 3398–3403.
97. Novet, T.; McConnell, J. M.; Johnson, D. C. *Chemistry of Materials* **1992**, *4*, 473–478.
98. Philophsky, E. M.; Hilliard, J. E. *J. Appl. Phys.* **1969**, *40*, 2198–2205.
99. Schlesinger, M. E. *Chem. Rev.* **1990**, *90*, 607–627.
100. Holloway, K. L. Ph.D. thesis, Stanford University, 1989.
101. de Boer, F. R.; Boom, R.; Miedema, A. R. *Physica B* **1980**, *101B*, 294–319.
102. Jäger-Waldau, A.; Lux-Steiner, M.; Jäger-Waldau, R.; Burkhardt, R.; Bucher, E. *Thin Solid Films* **1990**, *189*, 339–345.
103. Fister, L.; Johnson, D. C. *J. Am. Chem. Soc.* (accepted).
104. Cahn, J. W.; Hilliard, J. E. *J. Chem. Phys.* **1959**, *31*, 688–699.
105. Brophy, J. H.; Rose, R. M.; Wulff, J. *Thermodynamics of Structure*; John Wiley & Sons: New York, 1964; Vol. 2, pp. 91–94.
106. Wells, A. F. *Structural Inorganic Chemistry;* 5th Ed.; Clarendon Press: Oxford, 1984; pp. 1–1382.
107. Sommer, F. *J. Therm. Anal.* **1988**, *33*, 15.
108. Jounel, B.; Mathieu, J. C.; Desre, P. C. R. *C. R. Acad. Sci., Ser. 3* **1968**, *266*, 773.
109. Gorelkin, O. S.; V., M. S. *Russ. J. Phys. Chem. (Engl. transl.)* **1971**, *45*, 1523.
110. Cheng, H. C.; Yew, T. R.; Chen, L. J. *J. Appl. Phys.* **1985**, *57*, 5246–5250.
111. Oswald, R. S.; Ron, M.; Ohring, M. *Solid State Comm.* **1978**, *26*, 883–887.